astro-ph/9906203 11 Jun 1999

DESY 99-073

The AMANDA Neutrino Telescope: Principle of Operation and First Results

E. Andres[10], P. Askebjer[4], S.W. Barwick[6], R. Bay[5], L. Bergström[4], A. Biron[2], J. Booth[6], A. Bouchta[2], S. Carius[3], M. Carlson[8], D. Cowen[7], E. Dalberg[4], T. DeYoung[8], P. Ekström[4], B. Erlandson[4], A. Goobar[4], L. Gray[8], A. Hallgren[11], F. Halzen[8], R. Hardtke[8], S. Hart[10], Y. He[5], H. Heukenkamp[2], G. Hill[8], P.O. Hulth[4], S. Hundertmark[2], J. Jacobsen[9], A. Jones[10], V. Kandhadai[8], A. Karle[8], B. Koci[8], P. Lindahl[3], I. Liubarsky[8], M. Leuthold[2], D.M. Lowder[5], P. Marciniewski[11], T. Mikolajski[2], T. Miller[1], P. Miocinovic[5], P. Mock[6], R. Morse[8], P. Niessen[2], C. Pérez de los Heros[11], R. Porrata[6], D. Potter [10], P. B. Price[5], G. Przybylski[9], A. Richards[5], S. Richter[10], P. Romenesko[8], H. Rubinstein[4], E. Schneider[6], T. Schmidt[2], R. Schwarz[10], M. Solarz[5], G.M. Spiczak[1], C. Spiering[2], O. Streicher[2], Q. Sun[4], L. Thollander[4], T. Thon[2], S. Tilav[8], C. Walck[4], C. Wiebusch[2], R. Wischnewski[2], K. Woschnagg[5], G. Yodh[6]

1) Bartol Research Institute, University of Delaware, Newark, DE, USA
2) DESY-Zeuthen, Zeuthen, Germany
3) Kalmar University, Sweden
4) Stockholm University, Stockholm, Sweden
5) University of California Berkeley, Berkeley, CA, USA
6) University of California Irvine, Irvine, CA, USA
7) University of Pennsylvania, Philadelphia, PA, USA
8) University of Wisconsin, Madison, WI, USA
9) Lawrence Berkeley Laboratory, Berkeley, CA, USA
10) South Pole Station, Antarctica
11) University of Uppsala, Uppsala, Sweden

Abstract: AMANDA is a high-energy neutrino telescope presently under construction at the geographical South Pole. In the Antarctic summer 1995/96, an array of 80 optical modules (OMs) arranged on 4 strings (AMANDA-B4) was deployed at depths between 1.5 and 2 km. In this paper we describe the design and performance of the AMANDA-B4 prototype, based on data collected between February and November 1996. Monte Carlo simulations of the detector response to down-going atmospheric muon tracks show that the global behavior of the detector is understood. We describe the data analysis method and present first results on atmospheric muon reconstruction and separation of neutrino candidates. The AMANDA array was upgraded with 216 OMs on 6 new strings in 1996/97 (AMANDA-B10), and 122 additional OMs on 3 strings in 1997/98.

Paper submitted to Astroparticle Physics

1 Introduction

Techniques are being developed by several groups to use high energy neutrinos as a probe for the highest energy phenomena observed in the Universe. Neutrinos yield information complementary to that obtained from observations of high energy photons and charged particles since they interact only weakly and can reach the observer unobscured by intervening matter and undeflected by magnetic fields.

The primary mission of large neutrino telescopes is to probe the Universe in a new observational window and to search for the sources of the highest energy phenomena. Presently suggested candidates for these sources are, for instance, Active Galactic Nuclei (AGN) and Gamma Ray Bursts (GRB). A neutrino signal from a certain object would constitute the clearest signature of the hadronic nature of that cosmic accelerator [1]. Apart from that, neutrino telescopes search for neutrinos produced in annihilations of Weakly Interacting Massive Particles (WIMPs) which may have accumulated in the center of the Earth or in the Sun. WIMPS might contribute to the cold dark matter content of the Universe, their detection being of extreme importance for cosmology [2]. Neutrino telescopes can be also used to monitor the Galaxy for supernova explosions [3] and to search for exotic particles like magnetic monopoles [4]. In coincidence with surface air shower arrays, deep neutrino detectors can be used to study the chemical composition of charged cosmic rays. Finally, environmental investigations – oceanology or limnology in water, glaciology in ice – have proved to be exciting applications of these devices [5, 7].

Planned high-energy neutrino telescopes differ in many aspects from existing underground neutrino detectors. Their architecture is optimized to achieve a large detection area rather than a low energy threshold. They are deployed in transparent "open" media like water in oceans or lakes, or deep polar ice. This brings additional inherent technological challenges compared with the assembly of a detector in an accelerator tunnel or underground cavities. Neutrinos are inferred from the arrival times of Cherenkov light emitted by charged secondaries produced in neutrino interactions. The light is mapped by photomultiplier tubes (PMTs) spanning a coarse three-dimensional grid.

The traditional approach to muon neutrino detection is the observation of upward moving muons produced in charged current interactions in the rock, water or ice below the detector. The Earth is used as a filter with respect to atmospheric muons. Still, suppression of downward-going muons is of top importance, since their flux exceeds that of upward-going muons from atmospheric neutrinos by several orders of magnitude.

An array of PMTs can also be used to reconstruct the energy and location of isolated cascades due to neutrino interactions. Burst-like events, like the onset of a supernova, might be detected by measuring the increased count rates of all individual PMTs.

Technologies for under*water* telescopes have been pioneered by the since decommissioned DUMAND project near Hawaii [9, 10] and by the Baikal collaboration [5, 8]. In contrast to these approaches, the AMANDA detector [13] uses deep polar ice as target and radiator. Two projects in the Mediterranean, NESTOR [11] and ANTARES [12], have joined the worldwide effort towards large-scale underwater telescopes. BAIKAL and AMANDA are presently taking data with first stage detectors.

The present paper describes results obtained with the first four (out of the current thirteen) strings of the AMANDA detector. The paper is organized as follows: In section 2 we give a general overview of the AMANDA concept. Section 3 summarizes the results obtained with a shallow survey detector called AMANDA-A. Section 4 describes the design of the first four strings of the deeper array AMANDA-B4. Calibration of time response and of geometry are explained in section 5. In section 6 we describe the simulation and reconstruction methods with respect to atmospheric muons and compare experimental data to Monte Carlo calculations. Section 7 demonstrates the performance of AMANDA-B4 operated in coincidence with SPASE, a surface air shower array. In section 8, the angular spectrum of atmospheric muons is derived and transformed into a dependence of the vertical intensity on depth. Section 9 describes the separation of first upward going muon candidates. Finally, a summary of the status of AMANDA and results is presented in section 10.

2 The AMANDA Concept

AMANDA (Antarctic Muon And Neutrino Detector Array) uses the natural Antarctic ice as both target and Cherenkov medium. The detector consists of strings of optical modules (OMs) frozen in the 3 km thick ice sheet at the South Pole. An OM consists of a photomultiplier in a glass vessel. The strings are deployed into holes drilled with pressurized hot water. The water column in the hole then refreezes within 35-40 hours, fixing the string in its final position. In our basic design, each OM has its own cable supplying the high voltage (HV) as well as transmitting the anode signal. The components under the ice are kept as simple as possible, all the data acquisition electronics being housed in a building at the surface. The simplicity of the components under ice and the non-hierarchical structure make the detector highly reliable.

Fig. 1 shows the current configuration of the AMANDA detector. The shallow array, AMANDA-A, was deployed at a depth of 800 to 1000 m in 1993/94 in an exploratory phase of the project. Studies of the optical properties of the ice carried out with AMANDA-A showed that a high concentration of residual air bubbles remaining at these depths leads to strong scattering of light, making accurate track reconstruction impossible [6]. Therefore, in the polar season 1995/96 a deeper array consisting of 80 OMs arranged on four strings (AMANDA-B4) was deployed at depths ranging from 1545 to 1978 meters, where the concentration of bubbles was predicted to be negligible according to extrapolation of AMANDA-A results. The detector was upgraded in 1996/97 with 216 additional OMs on 6 strings. This detector of 4+6 strings was named AMANDA-B10 and is sketched at the right side of fig. 1. AMANDA-B10 was upgraded in the season 1997/98 by 3 strings instrumented between 1150 m and 2350 m which fulfill several tasks. Firstly, they explore the very deep and very shallow ice with respect to a future cube kilometer array. Secondly, they form one corner of AMANDA-II which is the next stage of AMANDA with altogether about 700 OMs. Thirdly, they have been used to test data transmission via optical fibers.

There are several advantages that make the South Pole a unique site for a neutrino telescope:

- The geographic location is unique: A detector located at the South Pole observes the northern hemisphere, and complements any other of the planned or existing detectors.

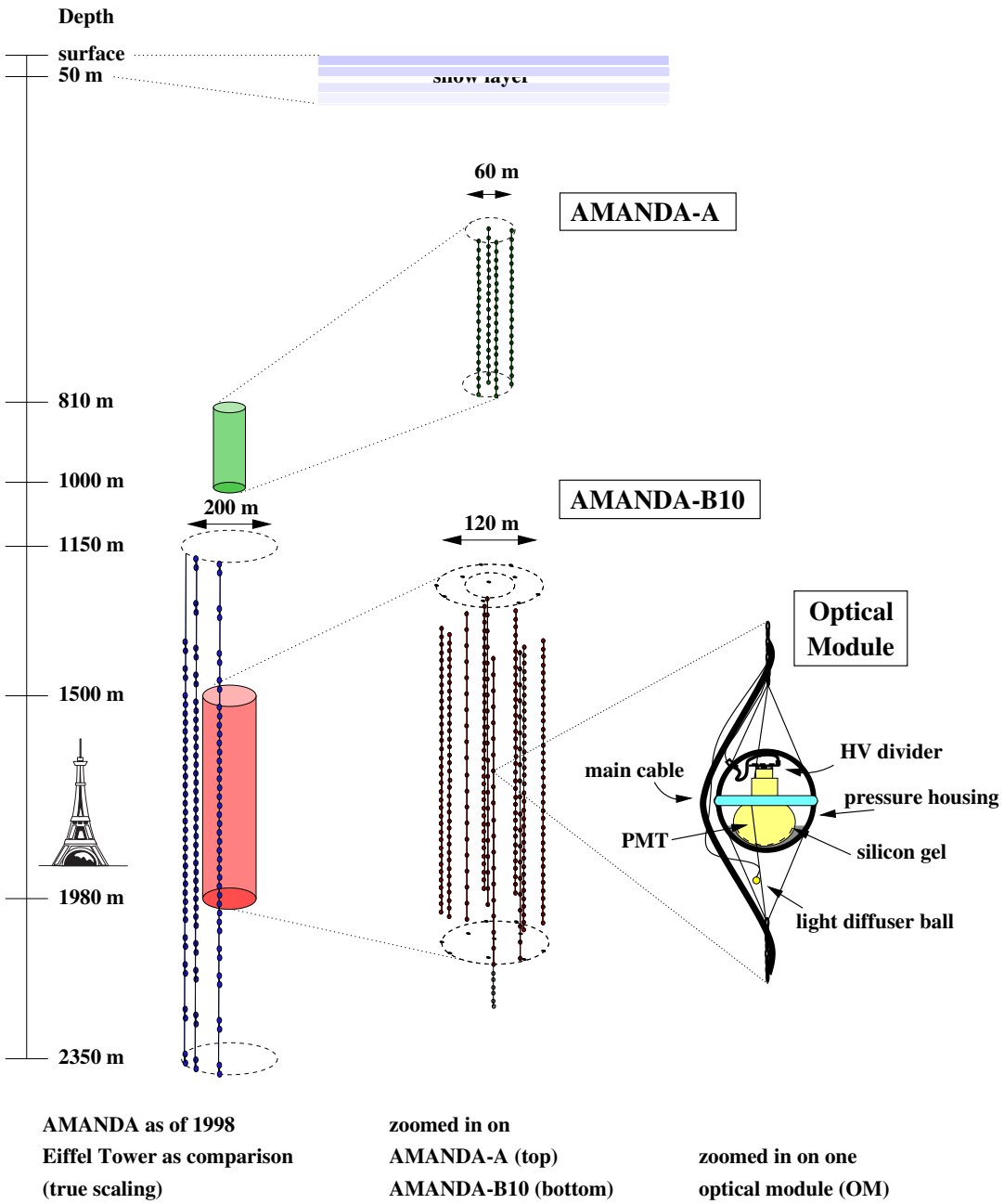

Figure 1: Scheme of the 1998 AMANDA installations. The left picture is drawn with true scaling. A zoomed view on AMANDA-A (top) and AMANDA-B10 (bottom) is shown at the center. The right zoom depicts the optical module.

- Ice is a sterile medium. The noise is given only by the PMT dark noise and by K^{40} decays in the glass housings, which are 0.5-1.5 kHz for the PMTs and spheres we used. Ocean and lake experiments have to cope with 100 kHz noise rates due to bioluminescence or K^{40} decays (25-30 kHz if normalized to the photocathode area of the 8″ PMT used in AMANDA). This fact not only facilitates counting rate experiments like the search for

low energy neutrinos from supernovae or GRBs, but also leads to fewer accidental hits in muon events – an essential advantage for trigger formation and track reconstruction.

- AMANDA can be operated in coincidence with air shower arrays located at the surface. Apart from complementing the information from the surface arrays by measurements of muons penetrating to AMANDA depths, the air shower information can be used to calibrate AMANDA.

- The South Pole station has an excellent infrastructure. Issues of vital importance to run big experiments like transportation, power supply, satellite communication and technical support are solved and tested during many years of operation. Part of an existing building can be used to house the surface electronics.

- The drilling and deployment procedures are tested and well under control. AMANDA benefits from the drilling expertise of the Polar Ice Coring Office (PICO). Currently about five days are needed to drill a hole and to deploy a string with PMTs to a depth of 2000 m. Future upgrades of the drilling equipment are expected to result in a further speed-up.

The optical properties of the ice turned out to be very different from what had been expected before the AMANDA-A phase. Whereas absorption is much weaker than in oceans, scattering effects turned out to be much stronger. Even at depths below 1400 meters, where residual bubbles have collapsed almost completely into air hydrates, scattering is nearly an order of magnitude stronger than in water (see below). Since scattering of light smears out the arrival times of Cherenkov flashes, a main question was whether under these conditions track reconstruction was possible. As shown below, the answer is yes.

3 AMANDA-A: A First Survey

Preliminary explorations of the site and the drilling technology were performed in the Antarctic Summer 1991/92 [13]. During the 1993/94 campaign, four strings each carrying 20 OMs ("AMANDA-A") were deployed between 800 and 1000 m depth. None of the 73 OMs (equipped with 8″ EMI PMTs) surviving the refreezing process failed during the following two years, giving a mean time between failures (MTBF) > 40 years for individual OMs in AMANDA-A. The OMs are connected to the surface electronics by coaxial cables. Along with the coaxial cables, optical fibers carry light from a Nd:YAG laser at the surface to nylon light diffusers placed about 30 cm below each PMT (see fig. 1). Time calibration is performed by sending nanosecond laser pulses to individual diffusers and measuring the photon arrival time distributions at the closest PMT. From the distribution of the arrival times at *distant* PMTs, the optical properties of the medium were derived [6, 7]. The measured timing distributions indicated that photons do not propagate along straight paths but are scattered and considerably delayed due to residual bubbles in the ice. The distributions could be fitted well with an analytic function describing the three-dimensional random walk (scattering) including absorption. These results showed that polar ice at these depths has a very large absorption length, exceeding 200 m at a wavelength of 410 nm. Scattering is described by the effective scattering length $L_{eff} = L_{sc}/(1 - \langle\cos\theta\rangle)$, where L_{sc} is the geometrical scattering length and $\langle\cos\theta\rangle$ the average cosine of the scattering angle [6].

L_{eff} increases with depth, from 40 cm at 830 m depth to 80 cm at 970 m. In accordance with measurements at the Vostok Station (East Antarctica [14]) and Byrd Station (West Antarctica) these results suggested that at depths greater than 1300-1400 m the phase transformation from bubbles into air-hydrate crystals would be complete and bubbles would disappear.

Although not suitable for track reconstruction, AMANDA-A can be used as a calorimeter for energy measurements of neutrino-induced cascade-like events [16]. It is also used as a supernova monitor [15]. Events that simultaneously trigger AMANDA-A and the deeper AMANDA-B have been used for methodical studies like the investigation of the optical properties of the ice or the assessment of events with a lever arm of one kilometer.

4 Deployment and Design of AMANDA-B4

4.1 Drilling and Deployment Procedure

Drilling is performed by melting the ice with pressurized water at 75°C. The drilling equipment operates at a power of 1.9 MW and the typical drill speed is about 1 cm/s. It takes about 3.5 days to drill a 50-60 cm diameter hole to 2000 m depth.

In the season 1995/96, we drilled four holes, the deepest of them reaching 2180 m. It took typically 8 hours to remove the drill and the water recycling pump from the completed hole. The deployment of one string with 20 OMs and several calibration devices took about 18 hours (with a limit of 35 hours set by the refreezing of the water in the hole).

Several diagnostic devices allow monitoring of the mechanical and thermal parameters during the entire refreezing process and afterwards. It was shown that the temperature increases with depth in good agreement with the prediction of a standard heat flow calculation for South Pole ice. At the greatest depth, the temperature of the ice is $\approx$ -31°C, about 20° warmer than at the surface. During the refreezing, the pressure reached a maximum of 460 atm, more than twice the hydrostatic pressure which is asymptotically established.

4.2 Detector Design

The four strings of AMANDA-B4 were deployed at depths between 1545 and 1978 m. An OM consists of a 30 cm diameter glass sphere equipped with a 8″ Hamamatsu R5912-2 photomultiplier, a 14-dynode version of the standard 12-dynode R5912 tube. The PMTs are operated at a gain of 10^9 in order to drive the pulses through 2 km of coaxial cable without in-situ amplification. The amplitude of a one-photoelectron pulse is about 1 V. The coaxial cable is also used for the HV supply, with the advantage that only one cable and one electrical penetrator into the sphere are required for each OM. The measured noise rate of the AMANDA-B4 PMTs is typically 400 Hz (threshold 0.4 photoelectrons).

The photocathode is in optical contact with the glass sphere by the use of silicon gel. The transmission of the glass of the pressure sphere is about 90% in the spectral range between 400 and 600 nm; the 50% cutoff on the UV side is at about 365 nm. The glass spheres are designed to withstand pressures of about 660 atm.

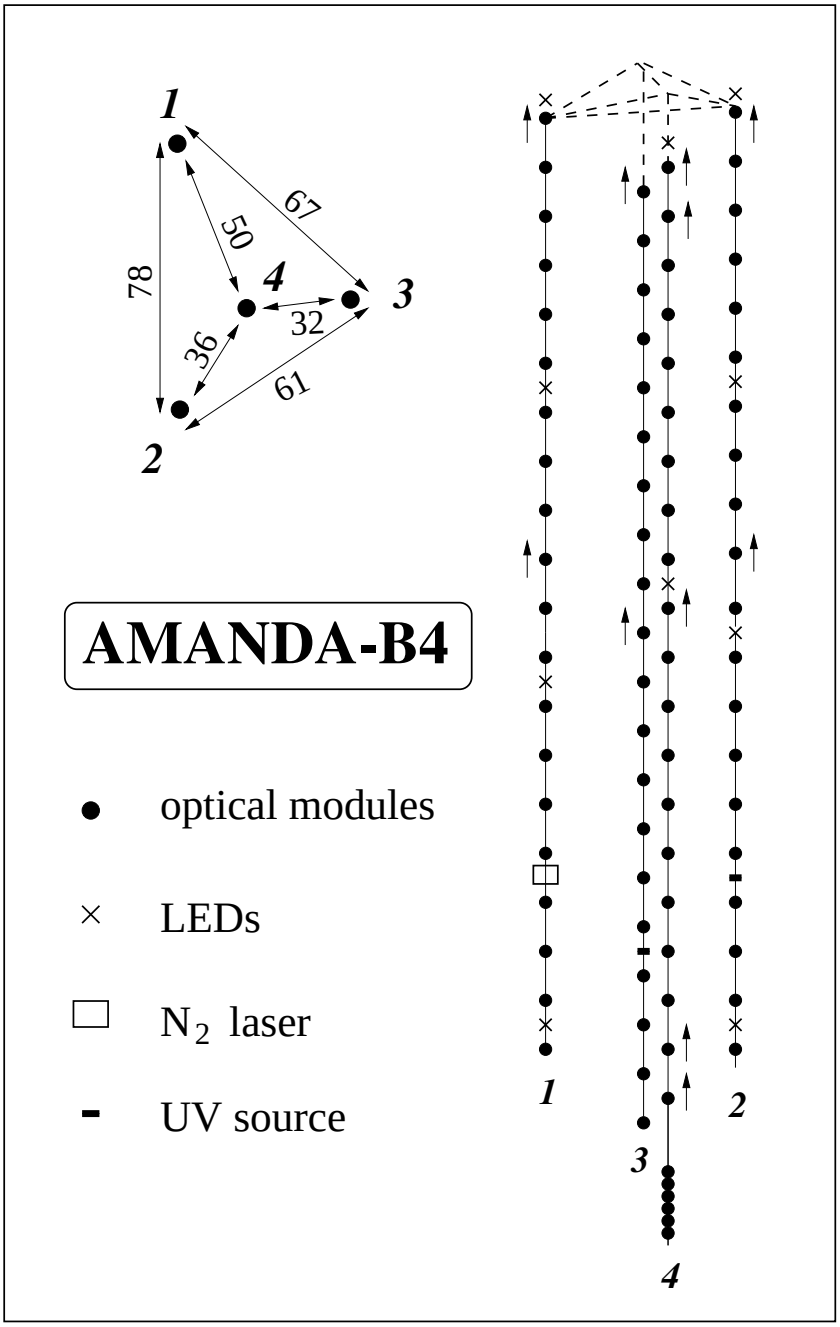

Figure 2: AMANDA-B4: Top view, with distances between strings given in meters, and side view showing optical modules and calibration light sources. Upward looking PMTs are marked by arrows.

Each string carries 20 OMs with a vertical spacing of 20 m. The fourth string carries six additional OMs connected by a twisted pair cable. These six OMs will not be used in the analyses presented in this paper.

Fig. 2 shows a schematic view of AMANDA-B4. All PMTs look down with the exception of # 1,10 in strings 1 to 3 and #1,2,10,19,20 in string 4 (with the numbers running from top to bottom of a string). Strings 1-3 form a triangle with side lengths 77-67-61 m; string 4 is close to the center. The OMs are arranged at depths 1545–1925 m (string 1), 1546–1926 m (string 2), 1598–1978 m (string 3) and 1576–1956 m (string 4). The additional six OMs equipped with twisted pair cables are at string 4 between 2009 and 2035 m. Seven of the 80 PMTs which define AMANDA-B4 were lost due to overpressure and shearing forces to the electrical connectors during the refreezing period. These losses can be reduced by computer controlled drilling avoiding strong irregularities in the hole diameter, and by improved connectors. Another 3 PMTs failed in the course of the first 3 years of operation, giving a MTBF of 73 years.

4.3 Electronics and DAQ

Each PMT can give a series of pulses which can be resolved if separated from each other by more than a few hundred nanoseconds. The data recorded consist of the leading and trailing edges of the pulses. The time-over-threshold gives a measure of the amplitude of individual pulses. Another measure of the amplitude is obtained by a voltage sensitive ADC which records the peak value out of the subsequent hits of an event in a PMT. Actually, the information consists of leading and trailing edges of the last 8 resolved pulses, and of the largest amplitude of those of them which lie in a 4 μsec window centered at the array trigger time. Also recorded is the GPS time at which the event occurred. A scheme of the AMANDA electronics layout is shown in fig. 3.

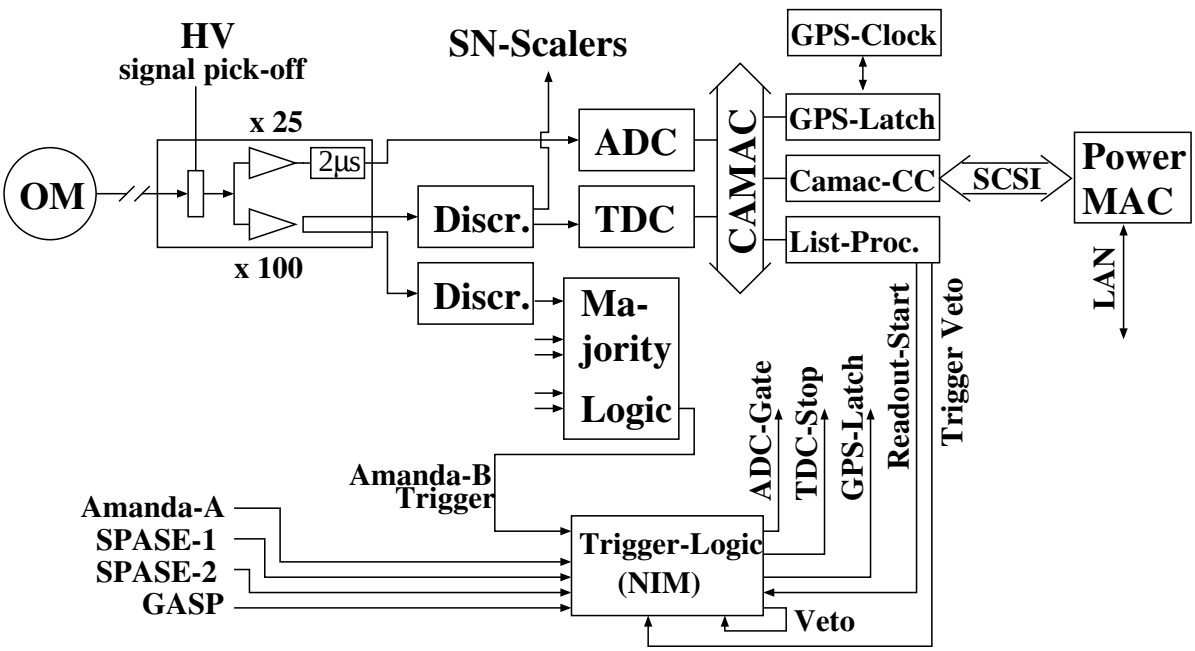

Figure 3: DAQ system used for AMANDA-B4 during 1996

The signal from each cable is fed to a module consisting of a DC blocking high-pass filter which picks up the pulse, a fan-out sending it to 2 amplifiers with $100\times$ and $25\times$ gain, and a 2 μsec delay for the low-gain signal.

The delayed signal is sent to a Phillips 7164 peak sensing ADC. The other pulse is split and sent to LeCroy 4413 discriminators with thresholds set at 100 mV corresponding to about 0.3-0.4 photoelectrons at the given high voltage. One of the resulting ECL pulses is fed into a LeCroy 3377 TDC while the other is sent to the majority trigger. The TDC records the last 16 time edges occurring within a 32 μsec time window.

The majority logic requests $\geq$ 8 hit PMTs within a sliding window of 2 μsec. The trigger produced by this majority scheme is sent to the NIM trigger logic. The latter accepts also triggers from AMANDA-A or the air shower experiments SPASE-1, SPASE-2 and GASP. Thus AMANDA also records data when these detectors trigger even if a proper AMANDA trigger is not fulfilled. The total trigger rate during 1996 was about 26 Hz on average. The coincidences from the other detectors contributed about 8 Hz to the total rate.

The differences in cable length are not compensated before triggering. Therefore the true trigger window would be about 300 nsec for a vertically downgoing relativistic particle and $\approx 4\mu$sec for an upgoing one. As a result downgoing particles are suppressed compared to upgoing.

Upon triggering, an ADC gate of 4 μsec width is formed, a stop signal is sent to the TDCs and a readout signal is sent to a Hytec LP1341 list processor. Then a veto lasting several microseconds inhibits further trigger signals.

A separate system ("SN scalers" in fig. 3) monitors the counting rates of individual PMTs and searches for rate excesses lasting several seconds. Such an increase would be expected for multiple low-energy neutrino interactions close to each PMT due to a supernova burst [3, 15].

The AMANDA-B4 DAQ was running on a MacIntosh Power PC communicating through a SCSI bus with the CAMAC crate controller. From the distribution of the time differences between subsequent events, the dead time of the DAQ is estimated to be about 12 %. The MacIntosh has been replaced by a Pentium-II PC running under LINUX in 1998, and part of the CAMAC electronics by VME modules.

Fig. 4 shows the distribution of the leading-edge times of one PMT for data taken with the 8-fold majority trigger. The sharp peak at 23 μsec is given by the time when this PMT was the triggering one (i.e. the eighth) within a 2μsec window. The flat part is due to noise hits and the bulge after the main distribution to afterpulses (about 6%.)

4.4 Calibration Light Sources and Ice Properties

An essential ingredient to the operation of a detector like AMANDA is the knowledge of the optical properties of the ice, as well as a precise time calibration of the detector. Various light calibration sources have been deployed at different depths in order to tackle these questions:

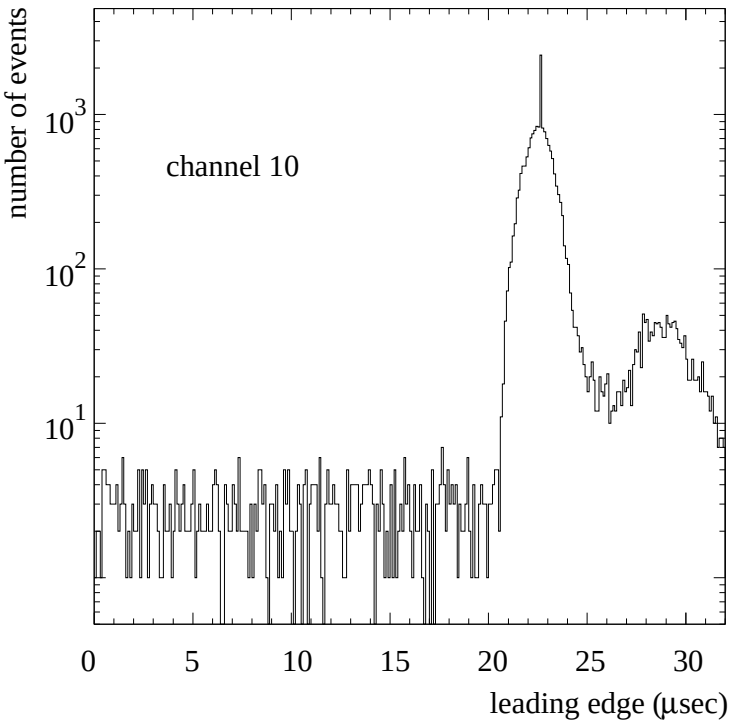

Figure 4: Leading edge times of PMT # 10 of AMANDA-B4 for data taken with an 8-fold majority trigger.

- **The YAG laser calibration system**. It uses optical fibers with diffusers located at each PMT. This system is similar to that used for AMANDA-A. The range of transmittable wavelengths is $\geq 450\,\mathrm{nm}$, the time resolution is about 15 nsec at 530 nm, the maximum intensity emitted by the diffusers is 10^8 photons/pulse. Apart from ice investigations, the laser system is used for time calibration of the PMT closest to the diffuser and for position calibration (see section 5).
- **A nitrogen laser** at 1850 m depth, wavelength 337 nm, pulse duration 1 nsec, with a maximum intensity of 10^{10} photons/pulse.
- **Three DC halogen lamps** (one broadband and two with filters for 350 and 380 nm), maximum intensity 10^{14} (UV-filtered) and 10^{18} (broadband) photons/second.
- **LED beacons**, operated in pulsed mode (500 Hz, pulse duration 7 nsec, 10^6 photons/pulse) and DC mode (10^{14} to 10^{15} photons/sec), wavelength 450 nm. A filter restricts the output of a few beacons to 390 nm, with reduced intensity.

Time-of-flight measurements have been made for a large variety of combinations of optical fiber emitters and PMTs for the YAG laser system, and at different wavelengths and intensities. The nitrogen laser provided data at 337 nm. The result is a considerable data base of hundreds of time distributions. The width of the distributions is sensitive predominantly to scattering and the tail to absorption (see [29] for details). The DC sources provide data for attenuation, i.e. the combined effect of absorption and scattering.

The YAG laser results indicate a dramatic improvement compared to AMANDA-A results. Fig. 5 shows the distributions of arrival time for source-detector distances of 20 and 40 m, respectively, for AMANDA-A as well as AMANDA-B depths. The much smaller widths for AMANDA-B support the expectation that bubbles as the dominant source of scattering have mostly disappeared at depths between 1550 and 1900 m [14].

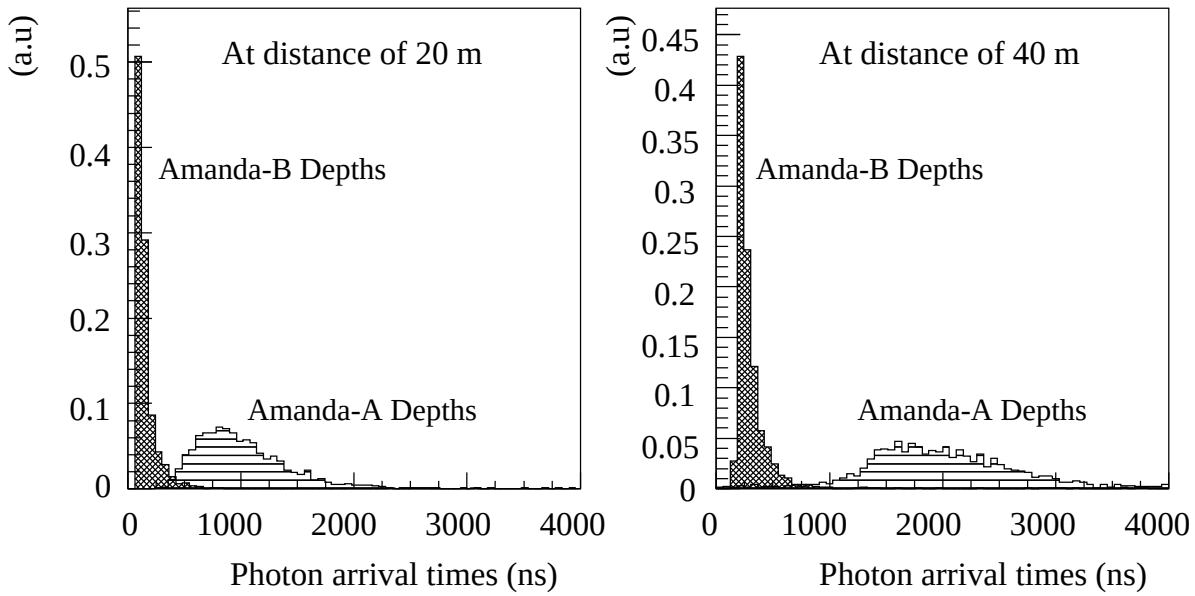

Figure 5: Arrival time distributions for 510 nm photons for two source-detector distances. Black histograms: AMANDA-B. Hatched histograms:AMANDA-A. The histograms are normalized to the same area.

Details of the analysis of the optical properties of the ice at AMANDA-B4 depths have been published elsewhere [17]. Final results will be published in a separate paper. Figure 6 shows preliminary data on the wavelength dependence of the coefficients for scattering, b_e, and absorption, a. The absorption length $\lambda_a = 1/a$ is between 90 and 100 m for wavelengths below 460 nm, i.e. ice does not degrade in transparency towards smaller wavelengths down to 337 nm. The effective scattering length $\lambda_{eff} = 1/b_e$ varies between 24 and 30 m in the relevant wavelength range. $\lambda_{eff} = \lambda_{scatt}/(1 - \langle\cos\theta\rangle)$, with λ_{scatt} being the geometric scattering length. $\langle\cos\theta\rangle$ is the average cosine of the scattering angle and is supposed to be about 0.8 in deep ice. The attenutation length λ_{att} which characterizes the decrease of the photon flux as a function of the distance is about 27 m. These values are averages over the full depth interval covered by AMANDA-B4. The variation of attenuation over this depth range is within $\pm 30\%$.

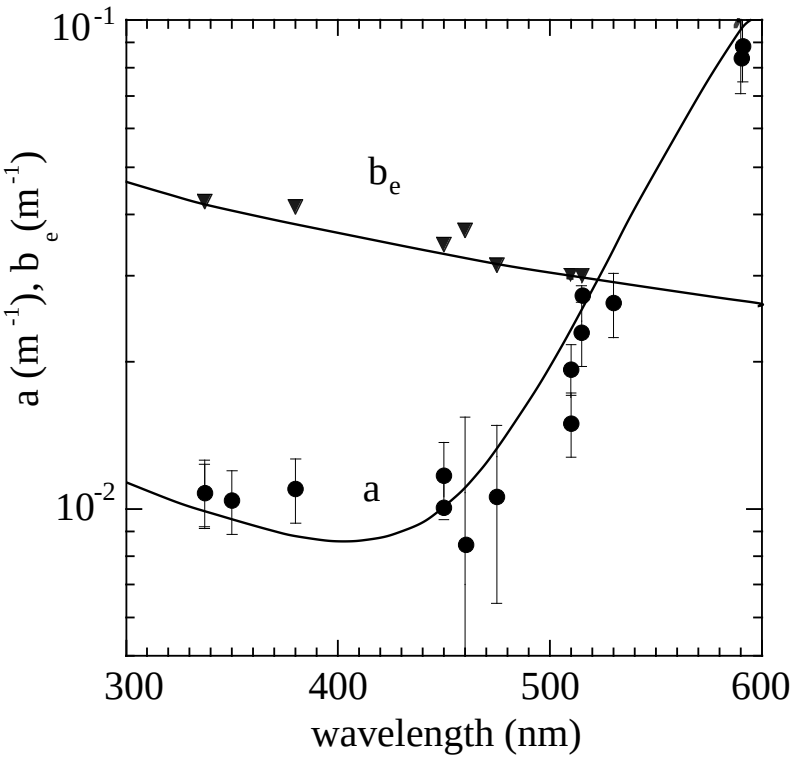

Figure 6: Absorption (a) and scattering (b_e) coefficients at an average depth of 1.7 km, compared to theory of He and Price [18].

5 Calibration of Time Response and Geometry

5.1 Time Calibration

The measured arrival times from each PMT have to be corrected for the time offset t_0, that is, the time it takes a signal to propagate through the PMT and the coaxial cable and get digitized by the DAQ. The time offset is determined by sending light pulses from the YAG laser to the diffuser nylon balls located below each OM. Two fibers are available for each PMT, one single and one multi-modal. The time it takes for light to travel though the fiber is measured using an OTDR (Optical Time Domain Reflectometer) and subtracted from the time distributions recorded.

For each PMT, the time difference between the laser pulse at the surface and the PMT response arriving back is measured. Upon arrival at the surface, the pulses have traveled through nearly 2000 meters of cable and are dispersed, with typical time-over-thresholds of 550 nsec and rise times of 180 nsec. The threshold used for TDC measurements is set to a constant value with the consequence that small pulses will reach that value later than larger ones. This causes an amplitude-dependent offset or "time walk", which can be corrected for by

$$t_{true} = t_{LE} - t_0 - \alpha/\sqrt{ADC}. \quad (1)$$

Here, t_{LE} is the measured leading edge time and t_{true} the true time at which the light pulse reaches the photocathode. The estimates of the time offset t_0 and the time-walk term α are extracted from scatterplots like the one shown in fig. 7.

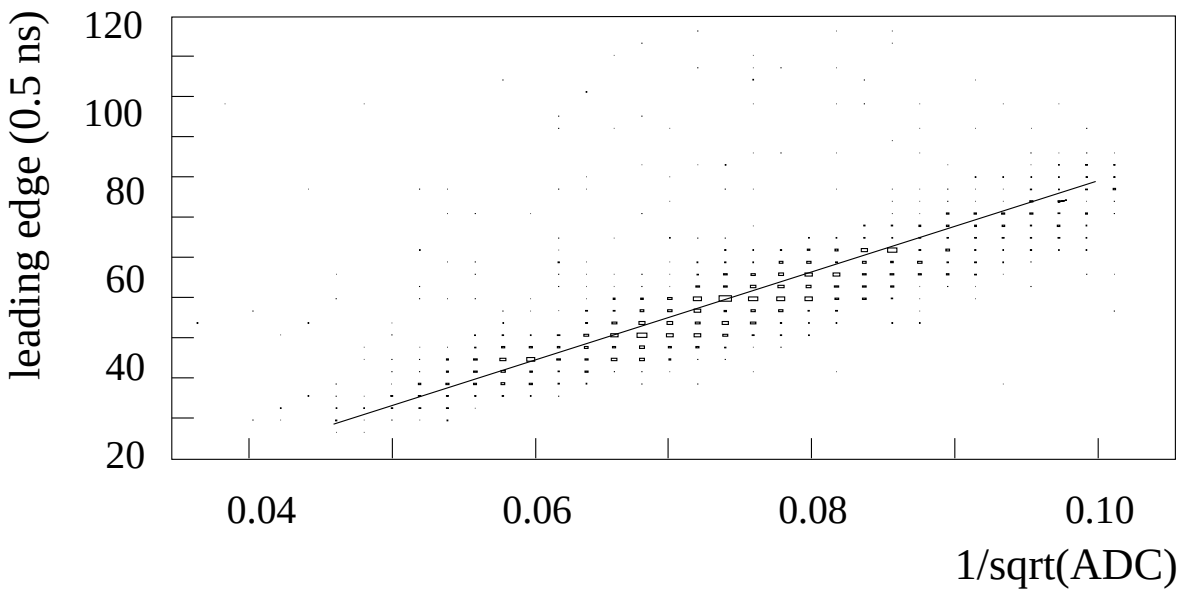

Figure 7: Example of a fitted leading edge (with 100<ADC<1200) for module 19 on string 3. The ADC value measures the peak value of the amplitude.

The time resolution achieved in this way can be estimated by the standard deviation of a Gaussian fit to the distribution of time residuals after correction, yielding 4–7 nsec (see Fig. 8 for an OM with 4 nsec resolution). Part of the variation is due to quality variations of the 1996 optical fibers. Laboratory measurements yield a Gaussian width of 3.5 nsec after 2 km cable.

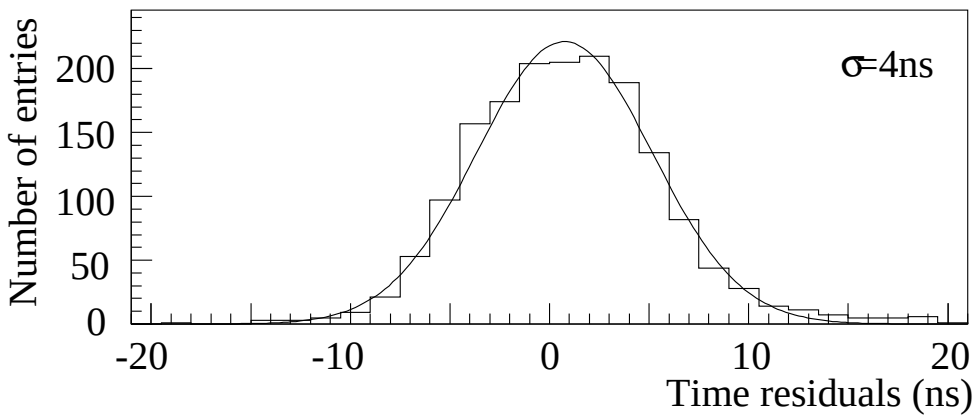

Figure 8: Residuals after subtracting the time correction obtained with the fitted parameters t_0 and α for module 19 on string 3. The standard deviation of the Gaussian fit is 4 nsec.

5.2 Position Calibration

Information about the exact geometry of the array can be obtained by different methods. Firstly, the measured propagation times of photons between different light emitters and receivers can be used to determine their relative positions. Secondly, absolute positions can be obtained from drill recordings and pressure sensors.

Laser Calibration

The YAG laser, the nitrogen laser and the pulsed LEDs can be used to infer the OM positions from the time-of-flight of photons between these light sources and the OMs. The zero time is determined from the response of the OM closest to the light source which is triggered by unscattered photons. This PMT is lowered in voltage in order not to be driven in saturation, and a time correction accounting for the longer PMT transit time is added. In contrast to the close OM, the distant OMs see mostly scattered photons. However, for a few of the events out of a series of about 1500 laser pulses, the leading edge should be produced by photons which are only slightly scattered. Therefore the distance between emitter and OM can be estimated from the earliest events in the time-difference distribution (see fig. 9).

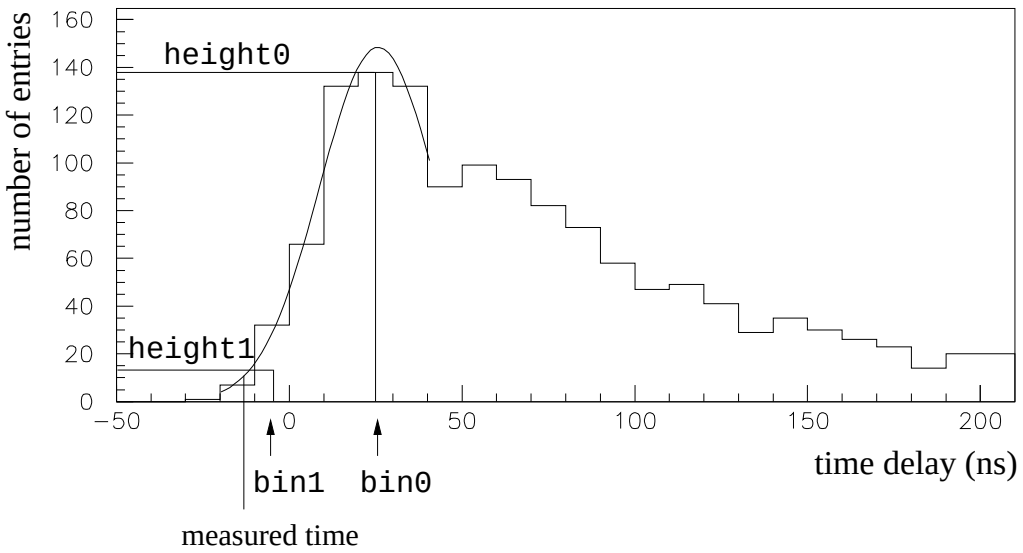

Figure 9: Simulated time-shift distribution for 1500 one-photoelectron events, for a distance of 60 m between emitter and receiver. A Gaussian smearing of 10 nsec was applied to individual entries. Clear ice would yield a 10 nsec wide peak at 0 nsec.

In order to reduce the sensitivity to fluctuations in the number of early hits and binning effects, the whole left flank of the distribution is fitted with a Gaussian between the maximum of the distribution (`height0` in fig. 9) and the first bin with a height larger than `height1` =1/10 `height0`. The corrected "first" time is given by that bin (`bin1`) for which the fitted Gaussian yields a height exceeding `height1`. This time has to be corrected further for the shifts due to scattering which are expected even for the first bin of the distribution. The corrections

were obtained from Monte Carlo (MC) calculations and are almost insensitive to variations in absorption and scattering length of a few meters.

Given the limited number of measured emitter-OM combinations available for AMANDA-B4, it would have been impossible to keep the coordinates of each OM as free parameters in a global position fit. Therefore, all strings were assumed to be straight and parallel and the OMs to be at a fixed vertical distance (20 m) relative to each other. For each emitter covering enough OMs, a graph of the distance $d(z_i)$ between source and OM i versus depth z_i can be drawn (see fig. 10). The inter-string distance D and emitter depth z_0 with respect to the z_i can be estimated from this graph by fitting (fig. 11):

$$d(z_i) = \sqrt{D^2 + (z_i - z_0)^2}. \tag{2}$$

The residuals from all fits to the 1996 AMANDA-B4 data have a standard deviation of 2 m.

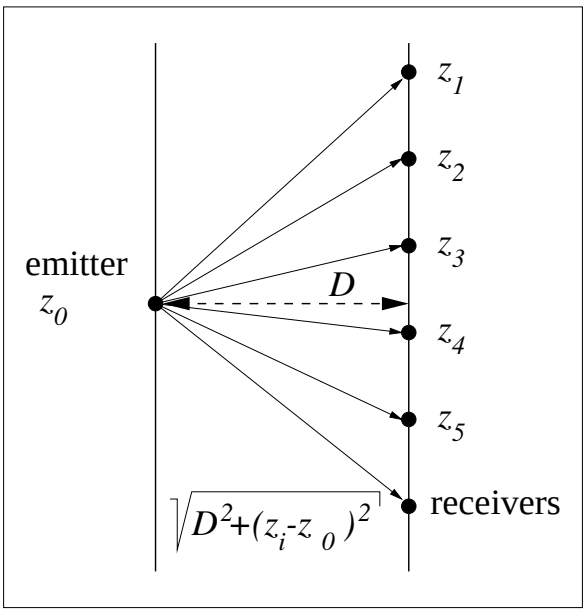

Figure 10: Principle of position measurement

In 1996–1997, six more strings were added on the outside of the B4 detector, and a new position calibration performed. The increased statistics and possibilities of new cross-checks and constraints enabled correction of the existing geometry with an uncertainty of 1 m in the horizontal plane and 0.5-1.0 m in depth.

Drill data

The geometry of the array is surveyed in an independent way by monitoring the position of the drill-head while it is going down each hole. The data were recorded by the drill instrumentation at each 10 cm step, recording the path-length, the value of the Earth's magnetic field as measured

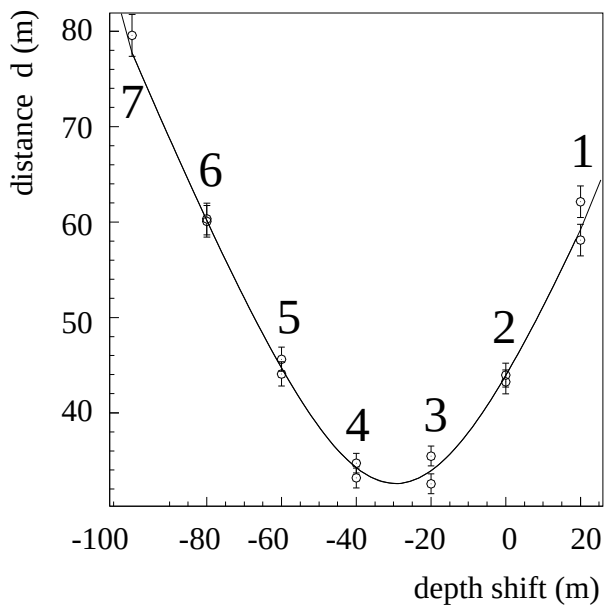

Figure 11: Fit of the distance $d(z_i)$ versus depth-shift $z_i - z_2$ between OMs at string 4 and a laser emitter at string 2. String distance D and depth shift $z_0 - z_2$ are given by the minimum of the parabola.

by a flux magnetometer and the angles (bank and elevation) given by perpendicular pendulums. This information can then be used to reconstruct the hole profiles. The results found are compatible with the laser measurements within 1-2 m in the horizontal plane. The advantage of this method is that it yields positions relative to the surface, i.e. in a global reference frame. It also takes into account tilts in the strings. However, it does not yield the depth locations of the OMs. The absolute depths of the strings were given by pressure sensors deployed with the OMs.

6 Simulation and Reconstruction of Muons

6.1 Simulation

Downgoing muons are generated by full atmospheric shower programs which simulate the production of muons by isotropic primary protons [19] or protons and nuclei [20] with energies up to 1 PeV. The muons are propagated down to a plane close to the detector. Upgoing muons are generated from atmospheric neutrinos, using the flux parameterization given in [21], from neutralinos annihilating in the center of the Earth, using the flux calculations of [2], and from point sources, using arbitrary energy distributions and source angles; they may start anywhere within the fiducial volume (which increases with increasing neutrino energy due to the muon range) and are propagated simulating the full stochastic energy loss according to [22].

It would be computationally impractical to generate and follow the path of each of the multiply scattered Cherenkov photons produced by muons and secondary cascades for every simulated event. Therefore, this step is accomplished by doing the photon propagation only once by a separate MC program and storing the results in large multidimensional tables. The tables give the distribution of the mean number of photoelectrons expected and of the time delay distribution, as a function of the position and the orientation of a PMT relative to the muon track. They include the effects of the wavelength dependent quantum efficiency, the transmission coefficients of glass spheres and optical gel, and the absorption and scattering properties of the ice. Once the tables are compiled, events can be simulated quickly by locating the PMT relative to any input particle and looking up the expected number and time distribution of photoelectrons in the tables[1]. The known characteristics of the AMANDA PMTs, the measured pulse shapes, pulse heights and delays after signal propagation along the cables, and the effect of electronics are then used to generate amplitude and time information [23].

6.2 Reconstruction

The reconstruction procedure for a muon track consists of five steps:

1. Rejection of noise hits, i.e. hits which have either a very small ADC value or which are isolated in time with respect to the trigger time or with respect to the nearest hit OM.
2. A line approximation following [24] which yields a point on the track, $\vec{r}$, and a velocity $\vec{v}$:

$$\vec{r} = \langle r_i \rangle - \vec{v} \cdot \langle t_i \rangle \qquad\qquad \vec{v} = \frac{\langle \vec{r_i} t_i \rangle - \langle \vec{r_i} \rangle \langle t_i \rangle}{\langle t_i^2 \rangle - \langle t_i \rangle^2}.$$

   with $\vec{r_i}$ and t_i being the coordinate vector and response time of the i-th PMT.
3. A likelihood fit based on the measured times which takes the the track parameters obtained from the line fit as start values. This "time fit" yields angles and coordinates of the track as well as a likelihood $\mathcal{L}_{time}$.
4. A likelihood fit using the fitted track parameters from the time fit and varying the light emission per unit length until the probabilities of the hit PMTs to be hit and non-hit PMTs to be not hit are maximized. This fit does not vary the direction of the track but yields a likelihood $\mathcal{L}_{hit}$ with can be used as a quality parameter.
5. A quality analysis, i.e. application of cuts in order to reject badly reconstructed events.

Steps 3 and 5 are outlined in the following two subsections.

6.3 Time Fit

In an ideal medium without scattering, one would reconstruct the path of minimum ionizing muons most efficiently by a χ^2 minimization process. Due to scattering in ice, the distribution

[1] This method assumes that ice is isotropic and and homogeneous which is reasonable in a first approximation: firstly, since the variations of the original ice with depth have been measured to be smaller than $\pm 25\%$, secondly, since the freshly frozen ice in the holes occupies only a small volume of the array.

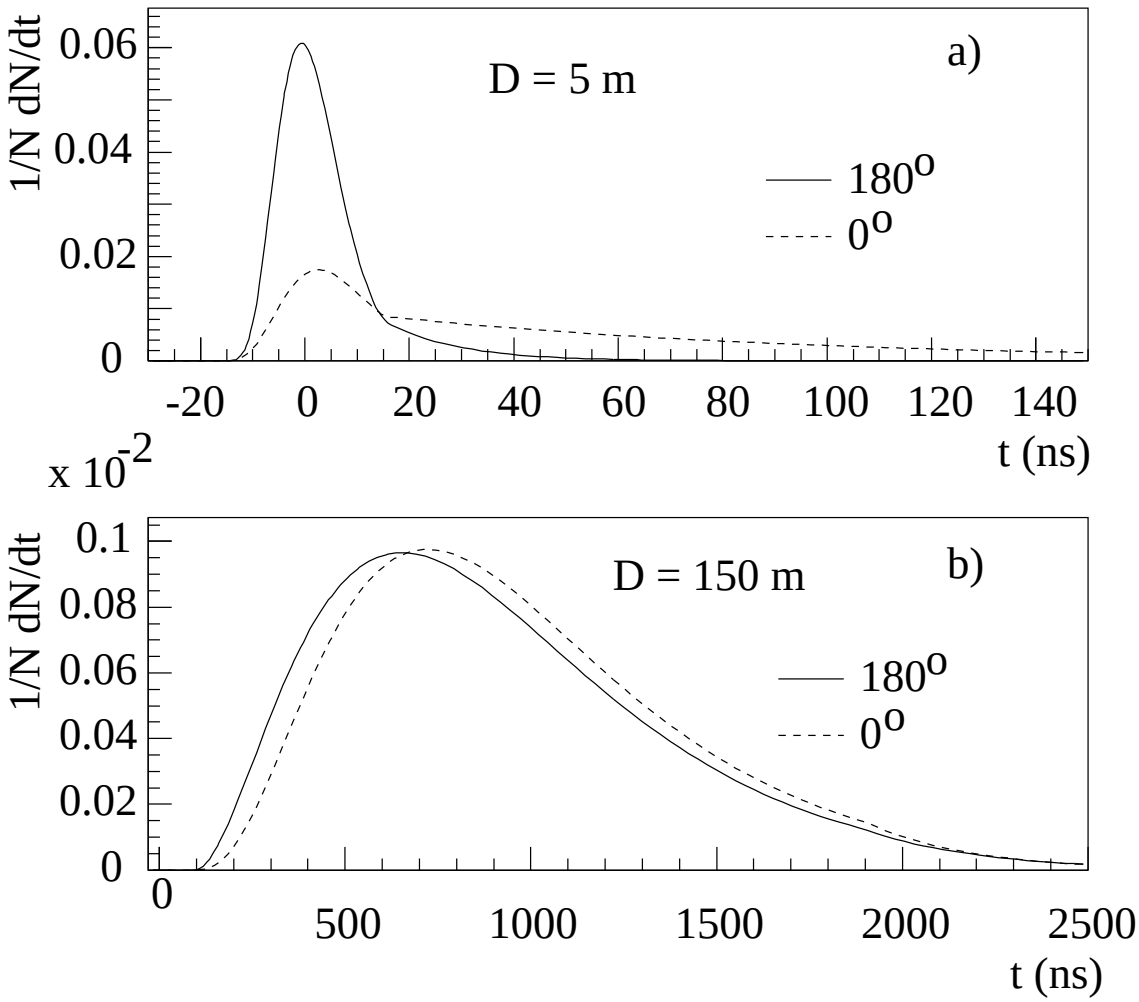

Figure 12: Delay-time distributions for modules facing (full curves) and back-facing (dashed curves) a muon track. Data are shown for muon tracks with impact parameters of 5 meters (a) and 150 meters (b).

of arrival times of photoelectrons seen by a PMT is not Gaussian but has a long tail at the high side – see fig. 12.

To cope with the non-Gaussian timing distributions we used a likelihood analysis. In this approach, a normalized probability distribution function $p_i(t)$ gives the probability of a certain time delay t for a given hit i with respect to straightly propagating photons. This probability function is derived from the MC simulations based on the photon propagation tables introduced in section 6.1. The probability depends on the distance and the orientation of the PMT with respect to the muon track. By varying the track parameters the logarithm of a likelihood function $\mathcal{L}$ is maximized.

$$\log(\mathcal{L}) = \log\left(\prod_{\text{all hits}} p_i\right) = \sum_{\text{all hits}} \log(p_i)$$

In order to be used in the iteration process, the time delays as obtained from the separate photon propagation Monte-Carlo have to be parameterized by an analytic formula. The parameterization of the propagation model itself is extended to allow for timing errors of PMTs and electronics as well as the probability of noise hits at random times. The AMANDA collaboration has developed two independent reconstruction programs, which are based on different parameterizations of the photon propagation and different minimization methods [25, 28, 26]. The comparison of these algorithms and the use of different optical models show that the results of both methods are in good agreement with each other and do not depend on a fine-tuning of the assumed optical parameters. Fig. 12 shows the result of the parameterization of the time delay for two distances and for two angles between the PMT axis and the muon direction. At a distance of 5 m and a PMT facing toward the muon track, the delay curve is dominated by the time jitter of the PMT. However, if the PMT looks in the opposite direction, the contribution of scattered photons yields a long tail towards large delays. At distances as large as 150 m, distributions for both directions of the PMT are close to each other since all photons reaching the PMT are multiply scattered.

The parameterization used for most of the results presented in this paper is a Gamma distribution modified with an absorption term [27]

$$p(d,t) = N \cdot \frac{\tau^{-(d/\lambda)} \cdot t^{(d/\lambda - 1)}}{\Gamma(d/\lambda)} \cdot e^{-t/\tau + c_w \cdot t/X_0 + d/X_0} \ ,$$

with the distance r between OM and muon track, the scaled distance $d \approx 0.8/\sin(\theta_c) \cdot r$, the absorption length X_0 and only two parameters $\tau \approx 700$ ns and $\lambda \approx 50$ m.

The second approach uses an F-distribution with an exponential tail for large time-delays, which results in a comparable accuracy [25].

6.4 Quality Analysis

Quality criteria are applied in order to select events which are "well" reconstructed. The criteria define cuts on topological event parameters and observables derived from the reconstruction. Below we list those used in the following:

- Speed $|\vec{v}|$ of the line fit. Values close to the speed of light indicate a reasonable pattern of the measured times, values smaller than 0.1 m/nsec indicate an obscure time pattern.
- "Time" likelihood per hit PMT $\log(\mathcal{L}_{time})/N_{hit}$.
- Summed hit probability for all hit PMTs $\sum P_{hit}$.
- "Hit" likelihood normalized to all working channels, $\log(\mathcal{L}_{hit})/N_{all}$.

The latter two parameters are good indicators of whether the location of the fitted track, which relies exclusively on the time information, is compatible with the location of the hits and non-hits within the detector.

- Number of direct hits, N_{dir}, which is defined to be the number of hits with time residuals $t_i(\text{measured}) - t_i(\text{fit})$ smaller than a certain cut value. We use cut values of 15 nsec, 25 nsec and 75 nsec, and denote the corresponding parameters as $N_{dir}(15)$, $N_{dir}(25)$ and $N_{dir}(75)$, respectively. Increasing the time window leads to higher cut values in N_{dir} but allows a finer gradation of the cut.

  Events with more than a certain minimum number of direct hits (i.e. only slightly delayed photons) are likely to be well reconstructed. This cut turned out to be the most powerful cut of all [28].

- The projected length of direct hits onto the reconstructed track, L_{dir}. A cut in this parameter rejects events with a small lever arm.

- Vertical coordinate of the center of gravity, z_{COG}. Cuts on this parameter are used to reject events close to the borders of the array. Very distant tracks are not likely to be well reconstructed.

Fig. 13 shows the distribution of two of these observables, the number of direct hits within 15 nsec, $N_{dir}(15)$, and the summed hit probability $\sum P_{hit}$ of all hit channels. It demonstrates the good agreement between results from MC and experiment.

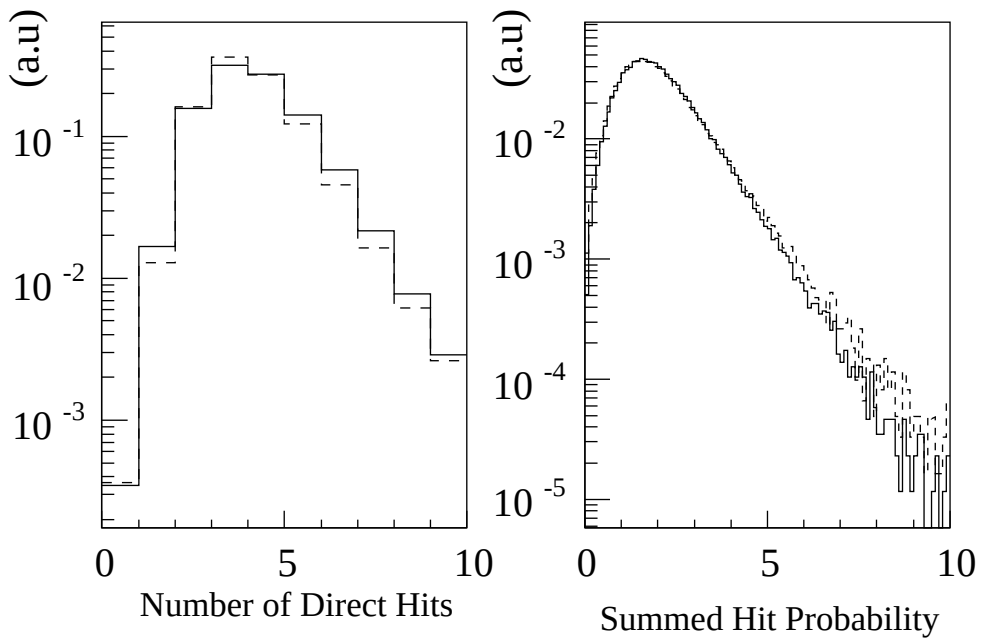

Figure 13: Distributions of two reconstructed event observables for MC down-going muon events (dashed lines) and from experimental data (full lines). *Left:* Number of direct hits, $N_{dir}(15)$; *Right:* summed hit probability, $\sum P_{hit}$,

Fig. 14 demonstrates the effect of cuts on the number of direct hits and the summed hit probability on the reconstructed angular distribution of experimental data and the MC sample. The cuts are $N_{direct}(15) \geq 5$ and $\sum P_{hit} \geq 2.5$. Both samples are dominantly due to down-going atmospheric muons. Despite that, a small but similar fraction of events is falsely reconstructed as up-going events. After application of the above quality criteria the tail below the horizon almost disappears. Note that not only the shapes but also the absolute passing rates on all cut levels are in good agreement between data and Monte Carlo. The angular mismatch between the reconstructed muon angle and the original angle used in the MC simulation after both cuts is 5.5 degrees. We note that this value strongly depends on the particular set of cuts, the minimum acceptable passing rate, the incident angle of the muon, and the range of muons stopping in the array.

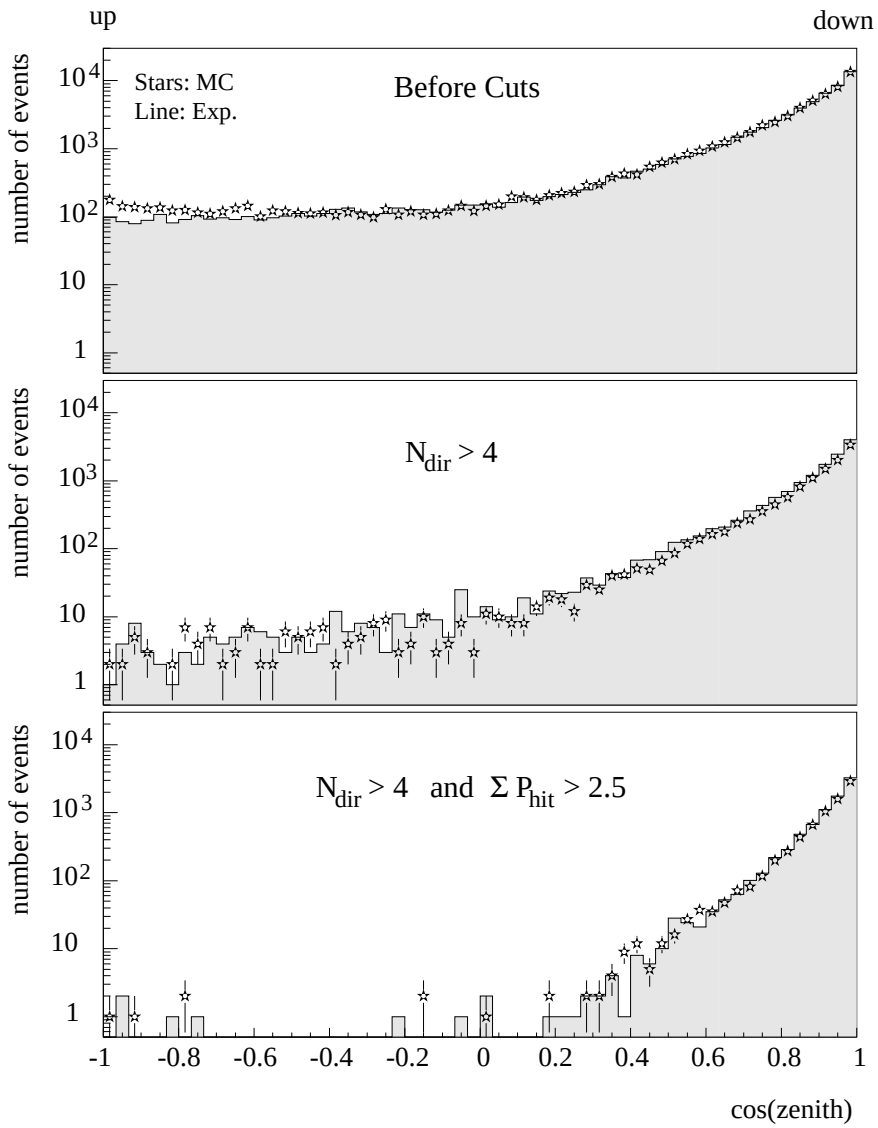

Figure 14: Reconstructed zenith angle distributions of experimental data (line) and downward muon MC events (points) after a stepwise application of quality cuts.

7 SPASE coincidences

AMANDA is unique in that it can be calibrated by muons with known zenith and azimuth angles which are tagged by air shower detectors at the surface. AMANDA-B4 has been running in coincidence with the two SPASE (South Pole Air Shower Experiment) arrays, SPASE-1 [33] and SPASE-2 [34]. SPASE-1 was located 840 m from the center of the AMANDA array projected to the surface, whereas SPASE-2 is located 370 m away (see fig.15). The scintillation detectors of SPASE-2 are complemented by an array of air Cherenkov detectors [30, 31]. The primary goal of these devices is the investigation of the chemical composition of primary cosmic rays in the region of the "knee" [32]. Another detector, the gamma imaging telescope GASP, is also operated in coincidence with AMANDA.

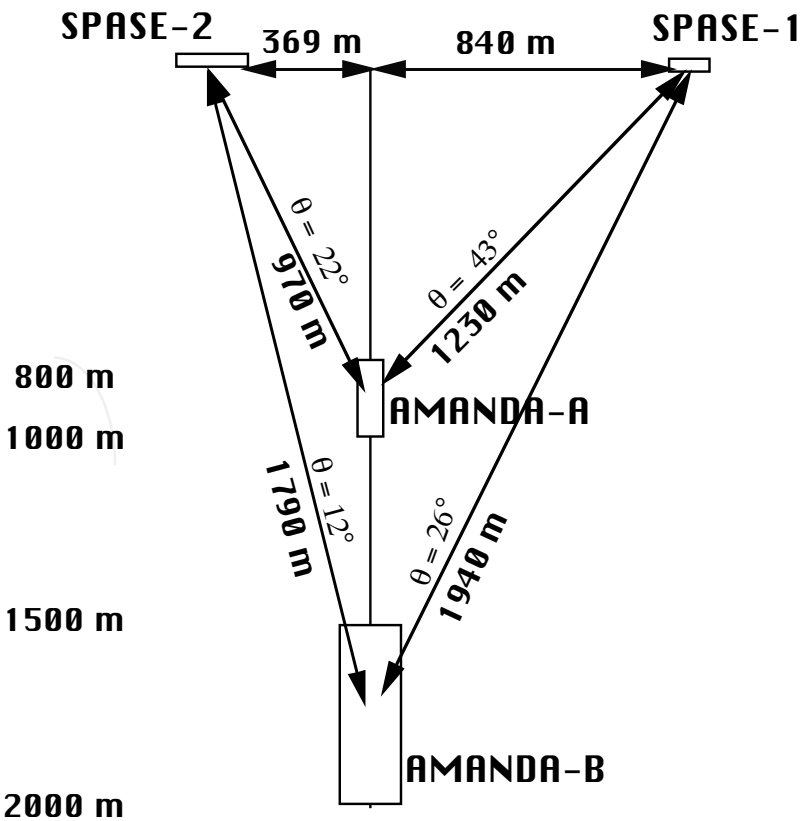

Figure 15: Side view of the two SPASE arrays relative to AMANDA-A and AMANDA-B.

In this section, we summarize calibration results obtained from the coincident operation of AMANDA and SPASE-2. SPASE-2 consists of 30 scintillator stations of $0.8\,\mathrm{m}^2$ on a 30 m triangular grid. The area of the array is $1.6 \cdot 10^4\,\mathrm{m}^2$, and it has been running since January 1996. For each air shower, the direction, core location, shower size and GPS time are determined. Showers with sufficient energy to trigger SPASE-2 ($\approx 100\,\mathrm{TeV}$) yield on average 1.2 muons penetrating to the depth of AMANDA-B. On every SPASE-1 or SPASE-2 trigger, a signal is sent to trigger AMANDA. The GPS times of the separate events are compared offline to match coincident events.

A one-week sample of these events has been analyzed in order to compare the directions of muons determined by AMANDA-B4 to those of the showers measured by SPASE-2. A histogram of the zenith mismatch angle between SPASE-2 and AMANDA-B4 is shown in fig.16. The selected events are required to have $\geq$8 hits along 3 strings and to yield a track which is closer than 150 m to the air shower axis measured by SPASE-2 (upper histogram). The hatched histogram shows the distribution of the zenith mismatch angle after application of the following quality cuts:

- likelihood $\log(\mathcal{L}_{time})/N_{hit} >$ -12,
- more than four hits with residuals smaller than 75 nsec ($N_{dir}(75) > 4$),
- length of the projection of OMs with direct hits to the track larger than 50 meters ($L_{dir}(75) > 50\,\mathrm{m}$).

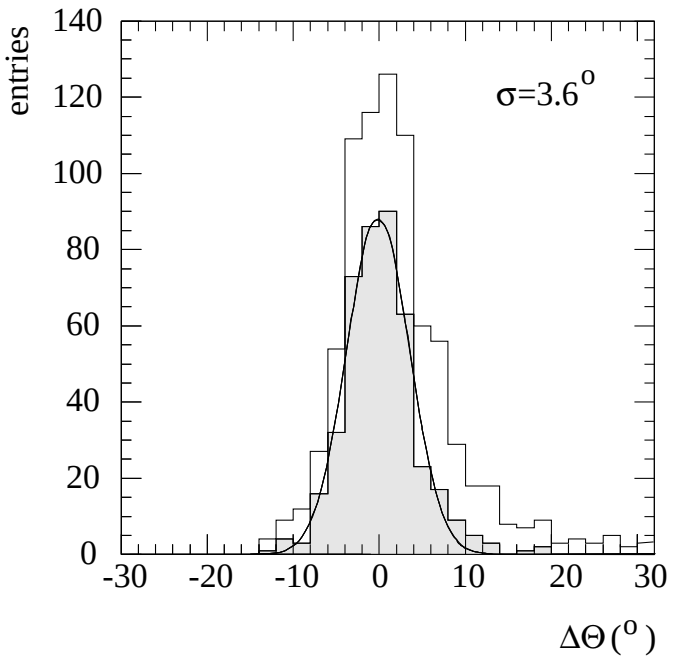

Figure 16: Mismatch between zenith angles determined in AMANDA-B4 and SPASE-2.

428 of the originally 840 selected events pass these quality cuts. The Gaussian fit has a mean of (0.14 ± 0.19) degrees and a width of $\sigma = (3.6 \pm 0.17)$ degrees. This is nearly 2 degrees better than the resolution obtained in the previous section for *all* downward muons and for a different set of cuts. MC yields a resolution of about 4 degrees.

The small mean implies that there is little systematic error in zenith angle reconstruction. The SPASE-2 pointing accuracy, which contributes to the average mismatch, depends on zenith angle and shower size. For most of the coincidence events, the SPASE-2 pointing resolution, defined as the angular distance within which 63% of events are contained, is between 1° and 2° [30, 31].

8 Intensity-vs-Depth Relation for Atmospheric Muons

8.1 Angular Dependence of the Muon Flux

In section 6, the muon angular distribution was shown as a function of various cuts in order to demonstrate the agreement between experimental data and MC simulations. In this section, we calculate the muon intensity I as a function of the zenith angle θ. $I(\theta_\mu)$ is given by

$$I(\theta_\mu) = \frac{S_{dead}}{T \cdot \Delta\Omega} \frac{N_\mu(\theta) \cdot m(\theta_\mu)}{\epsilon_{rec}(\theta_\mu) \cdot A_{eff}(\text{cut}, \theta_\mu)} \tag{3}$$

where

- $N_\mu(\theta)$ is the number of muons assigned by the analysis to a zenith angle interval centered around $\cos\theta_\mu$. For the analysis presented in this section, we start from the angular distribution $N_\mu(\theta_{rec})$ obtained from the reconstruction, without applying cuts. This distribution is strongly smeared (see fig. 14, top). We have calculated the elements of the parent angular distribution $N_\mu(\theta)$ from the reconstructed distribution $N_\mu(\theta_{rec})$ using a regularized deconvolution procedure [37, 36].
- T is the run time. We used the data from June 24, 1996, with $T = 22.03$ hours, and $9.86 \cdot 10^5$ events triggering AMANDA-B4.
- S_{dead} corrects for the dead time of the data acquisition system. This factor was determined from the time difference distribution of subsequent events. The dead-time losses for the two runs used in this analysis are 12%, i.e. $S_{dead} = 1/0.88 = 1.14$.
- $\Delta\Omega$ is the solid angle covered by the corresponding $\cos\theta_\mu$ interval.
- $A_{eff}(\text{cut}, \theta_\mu)$ is the effective area, after the application of a multiplicity trigger, for a given cut at zenith angle θ_μ. The effective area is shown in fig. 17 as a function of the zenith angle and for different cuts on the number of hit OMs.
- $\epsilon_{rec}(\theta_\mu)$ is the reconstruction efficiency for zenith angle θ_μ which ranges between 0.82 at $\cos\theta = 1.0$ and 0.75 at $\cos\theta = 0.2$.
- $m(\theta_\mu)$ is the mean muon multiplicity at angle θ_μ at the "trigger depth". The trigger depth h_{eff} was defined as depth of $\overline{z_{OM}}$, the center of gravity in the vertical coordinate z of all hit OMs. The average h_{eff} depends on the angle. It is highest for $\cos\theta$ between 0.4 and 0.8 (about 30 m below the detector center) and falls toward the vertical (at maximum 80 m below the center). The mean muon multiplicity is about 1.2 for vertical tracks and decreases towards the horizon. Since the generator used in this analysis [19] simulates only proton induced showers, this value is an underestimation by about 10%.

Fig. 18 shows the angular distribution of the flux of downgoing muons, $I(\theta_\mu)$, as obtained from eq.3. In order to illustrate the stability of the method with respect to cuts biasing the measured angular distribution, the flux is shown for samples defined by different majority triggers ($N_{hit} > 8, 10, 12, 14, 16, 18$). Apart from the point closest to the horizon which is not only most strongly biased but also has the lowest statistics, deviations are within 25%. For further studies we use the sample with $N_{hit} \geq 16$.

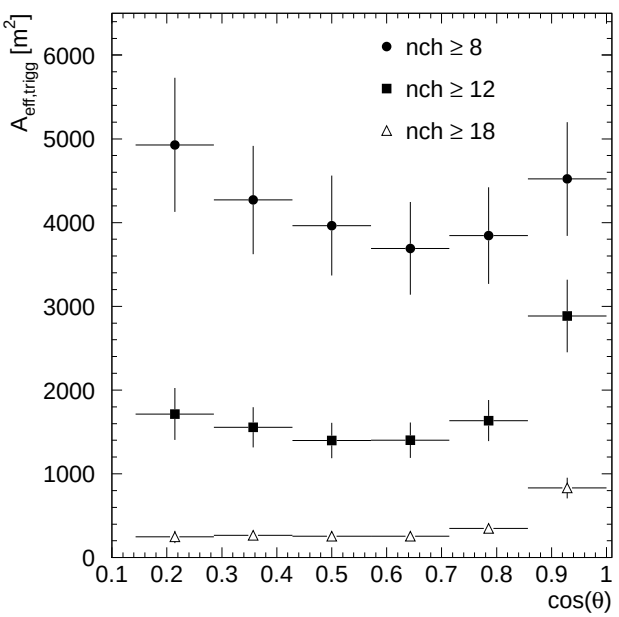

Figure 17: Effective trigger area of AMANDA-B4 as a function of zenith angle, for 3 different majority criteria.

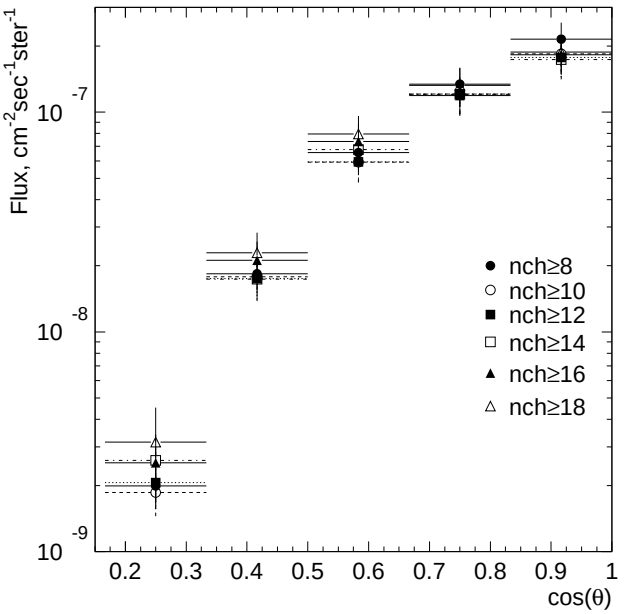

Figure 18: Angular distribution of the downward going muon flux, $I(\theta_\mu)$, as obtained from eq.(3).

8.2 Transformation of Angular Flux to Vertical Intensity as a Function of Depth

The measured flux $I(\theta)$ can be transformed into a vertical flux $I(\theta = 0, h)$, where h is the ice thickness seen under an angle θ:

$$I(\theta = 0, h) = I(\theta) \cdot \cos(\theta) \cdot c_{corr} \tag{4}$$

The $\cos\theta$-conversion correcting for the $\sec(\theta)$ behavior of the muon flux is valid for angles up to 60^o [46]. The term c_{corr} taken from [44] corrects for larger angles and lies between 0.8 and 1.0 for the angular and energy ranges considered here.

The vertical intensities obtained in this way are plotted in fig. 19 and compared to the depth-intensity data published by DUMAND [45] and Baikal [5], and to the prediction by Bugaev et al. [38]. One observes satisfying agreement of all experiments with the prediction.

We also fitted our data to a parameterization taken from [39, 40]:

$$I(h) = I_0 \cdot E_{crit}^{-\gamma} = I_0 \cdot \left(\frac{a}{b_{eff}} \cdot \left[e^{(b_{eff} \cdot h)} - 1 \right] \right)^{-\gamma} \tag{5}$$

E_{crit} is the minimum energy necessary to reach the depth h. It is obtained from the parameterization [46] $dE/dx = a + b \cdot E_\mu$ where $a \approx 2$ MeV/(g·cm^{-2}) denotes the continuous energy loss due to ionization, and $b(E_\mu)$ is proportional to the stochastic energy loss due to pair production, bremsstrahlung and nuclear cascades. From this parameterization one obtains $E_{crit} = a/b \cdot [\exp(b \cdot h) - 1]$. I_0 is the normalization parameter and $\gamma \approx 2.78$ [40] the spectral index. We approximate $b(E_\mu)$ by an energy independent parameter b_{eff}. Fitted to equation (5), our data for the vertical intensity result in the following values for I_0 and b_{eff}:

$$I_0 = (5.04 \pm 0.13)\,\mathrm{cm}^{-2}\mathrm{s}^{-1}\mathrm{ster}^{-1}$$
$$b_{eff} = (2.94 \pm 0.09) \cdot 10^{-6}\,\mathrm{g}^{-1}\,\mathrm{cm}^2.$$

This compares to $I_0 = (5.01 \pm 0.01)\,\mathrm{cm}^{-2}\mathrm{s}^{-1}\mathrm{ster}^{-1}$ and $b_{eff} = (3.08 \pm 0.06)\,10^{-6}\,\mathrm{g}^{-1}\,\mathrm{cm}^2$ obtained for $N_{hit} \geq 8$, showing that the result is rather insensitive to the actual cut condition.

For the purpose of completeness we give also the results for the more usual parameterization

$$I(h, \theta_\mu = 0) = a_\mu \left(\frac{\lambda}{h} \right)^\alpha \mathrm{e}^{-h/\lambda} \tag{6}$$

where α is set to 0 [41], to 2 [42] or is a free parameter [43]. The purely exponential dependence ($\alpha = 0$) clearly does not describe the data at depths smaller than 4-5 km. Leaving all parameters free [43], one obtains $a_\mu = (0.89 \pm 0.30) \cdot 10^{-6}\,\mathrm{cm}^{-2}\mathrm{s}^{-1}\mathrm{ster}^{-1}$, $\lambda = (1453 \pm 612)\,\mathrm{g\,cm}^{-2}$, and $\alpha = 2.0 \pm 0.25$, being also in agreement with α fixed as in [42].

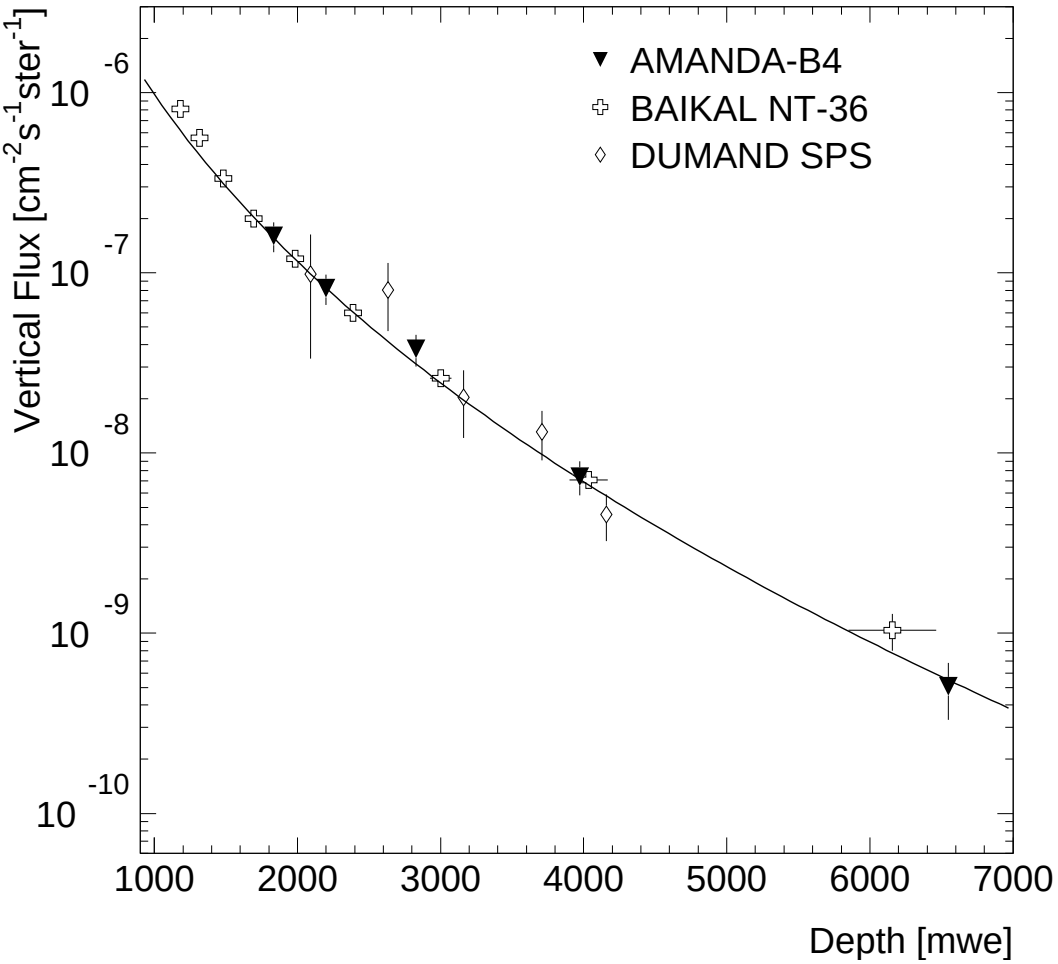

Figure 19: Vertical intensity versus depth for AMANDA, BAIKAL and DUMAND. The solid line gives the prediction of [38] which coincides with the curves obtained from the parameterizations (5) and (6).

9 Search for Upward Going Muons

AMANDA-B4 was not intended to be a full-fledged neutrino detector, but instead a device which demonstrates the feasibility of muon track reconstruction in Antarctic ice. The limited number of optical modules and the small lever arms in all but the vertical direction complicate the rejection of fake events. In this section we demonstrate that in spite of that the separation of a few upward muon candidates was possible.

We present the results of two independent analyses. One uses the approximation of the likelihood function by a F-function with an exponential tail [25], the other the approximation by a Gamma function with an absorption term [26] (see section 6.3).

Both analyses apply separation criteria which are obtained from a stepwise tightening of cuts on

different parameters, in a way which improves the signal-to-fake ratio given by the MC samples. Since the MC generated samples of downward-going muons (a few million events) run out of statistics after a reduction factor of about 10^6, further tightening of cuts is performed without background-MC control until the experimental sample reaches the same magnitude as the MC predicted signal.

For both analyses, the full experimental data set of 1996, starting with Feb.19th and ending with Nov.5th, was processed. It consists of $3.5 \cdot 10^8$ events.

Analysis 1

In a first step, a fast pre-filter reduced this sample to a more manageable size. It consists of a number of cuts on quickly computable variables which either correlate with the muon angle, or which to a certain degree distinguish single muons from the downgoing multi-muon background events like, e.g. a cut on the zenith angle from a line fit [24], cuts on time differences between OMs at different vertical positions, and topological cuts requesting a minimum vertical elongation of the event.

These cuts reduce the size of the experimental data sample to 5.2%, the simulated atmospheric muons to 4.8% and simulated up-going events to 49.8%.

Simulated up-going events and experimental data have been reduced by further cuts:

- At least 2 strings have to be hit (this condition relaxes the standard condition "$\geq$3 strings" and increases the effective area in the vertical direction).
- The events were reconstructed below horizon, i.e. $\theta > 90^o$.
- $\log(\mathcal{L}_{time})/N_{hit} > -6$.
- $\alpha \geq 0.15$ m/nsec, where α is obtained from a fit to $z_i = \alpha \cdot t_i + \beta$ and z_i, t_i being the z coordinates and times of the hit OMs.

Fig. 20 shows the distribution of the number of direct hits, $N_{dir}(15)$, of all events passing these cuts. The highest cut in N_{direct} survived by *any* experimental event is $N_{direct} \geq 6$. The two surviving events are shown in fig. 21. The Monte-Carlo expectation for upward muons from atmospheric neutrinos is 2.8 events, with an uncertainty of a factor 2, mostly due to uncertainties in the sensitivity of the detector after all cuts.

Analysis 2

The $3.5 \cdot 10^8$ experimental events were compared to $3.5 \cdot 10^6$ MC events from atmospheric down-going muons which correspond to 2 days effective live time. The MC data set for upward muons from atmospheric neutrino interactions [48] consists of $2.5 \cdot 10^3$ events triggering AMANDA-B4 – corresponding to 1.7 years effective live time.

In order to separate neutrino induced upward muons, we applied a number of successively tightened cuts in the variables defined in section 6.4. This procedure reduced the experimental sample to the expected signal sample after the following cuts:

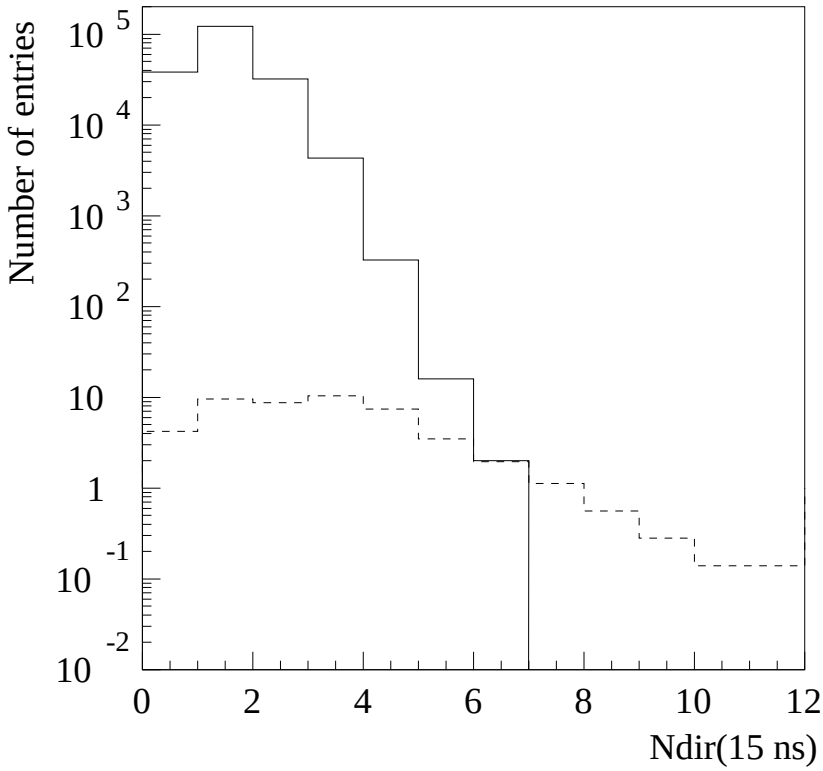

Figure 20: Number of events surviving pre-filter and additional cuts as a function of $N_{dir}(15)$. Solid line: 6-month experimental data. dashed line: 6-month expectation from atmospheric neutrinos.

1. reconstructed zenith angle $\theta > 120^o$,
2. speed of the line fit $0.15 < |\vec{v}| < 1$ m/nsec,
3. "time" likelihood $\log(\mathcal{L}_{time})/(N_{hit} - 5) > -10$ (i.e. normalizing to the degrees of freedom instead of the the number of hit PMTs),
4. "hit" likelihood $\log(\mathcal{L}_{hit})/(N_{hit} - 5) > -8$,
5. number of direct hits for 25 nsec window, $N_{dir}(25) \geq 5$,
6. number of direct hits for 75 nsec window, $N_{dir}(75) \geq 9$,
7. projected length of direct hits for 25 nsec window, $L_{dir}(25) > 200$ m,
8. absolute value of the vertical coordinate of the center of gravity $|z_{COG}| < 90$m (with the center of the detector defining the origin of the coordinate system).

Three events of the experimental sample passed these cuts, corresponding to a suppression factor of $8.9 \cdot 10^{-9}$. The passing rate for MC upward moving muons from atmospheric neutrinos is 1.3 % which corresponds to 4.0 events in 156 days. The corresponding enrichment factor is $0.013/(8.9 \cdot 10^{-9}) \approx 1.5 \cdot 10^6$. One of the three experimental events was identified also in the

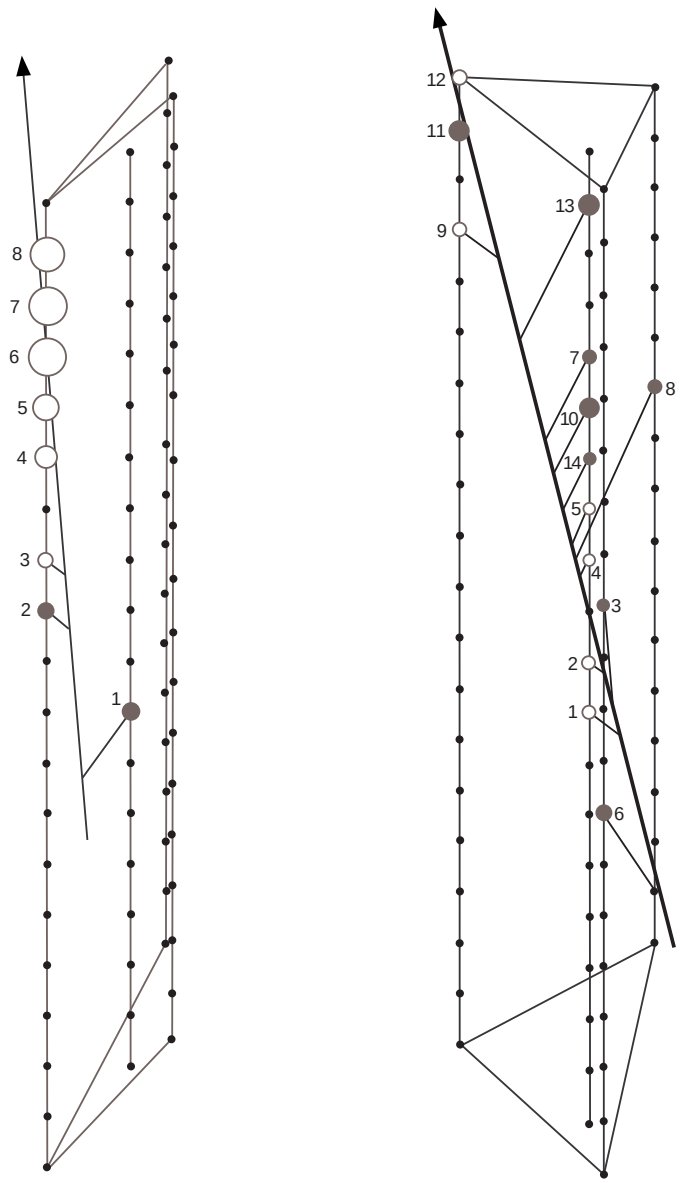

Figure 21: The two experimental events reconstructed as upward muons. *left:* ID 8427997, *right:* ID 4706870. The line with an arrow symbolizes the fitted muon track, the lines from this track to the OMs indicate light pathes. The amplitudes are proportional to the size of the OMs. The numbering of the OMs refers to the time order in which they are hit.

search from the previous subsection. A second event with $N_{dir} = 5$ passes all cuts of the previous analysis, with the exception of the N_{dir} cut.

In order to check how well the parameter distributions of the events agree with what one expects for atmospheric neutrino interactions, and how well they are separated from the rest of the experimental data, we relaxed two cuts at a time (retaining the rest) and inspected the distribution in the two "free" variables.

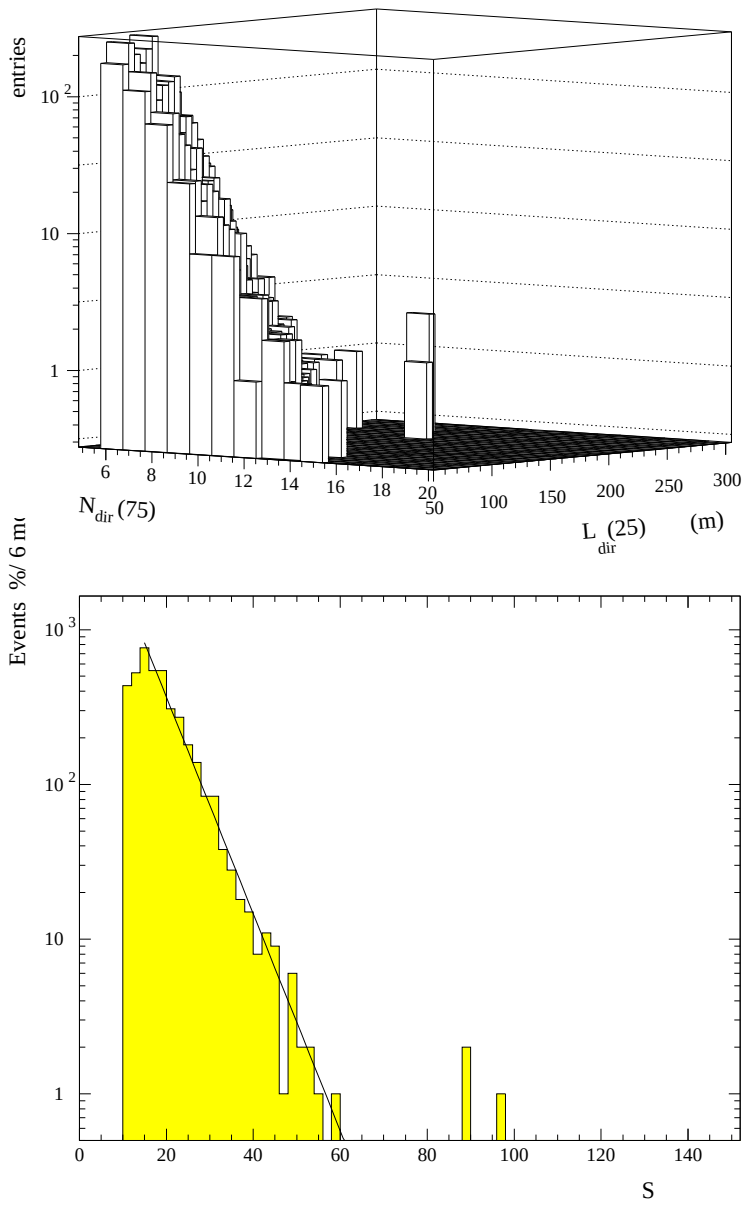

Figure 22: *Top* – distribution in parameters $L_{dir}(25)$ vs. $N_{dir}(75)$, *bottom:* distribution in the "combined" parameter $S = N_{dir}(75) \cdot L_{dir}(25)$ / 20. The cuts applied to the event sample include all cuts with the exception of cuts 6 and 7.

Fig. 22 shows the distribution in $L_{dir}(25)$ and $N_{dir}(75)$. The three events passing *all* cuts are separated from the bulk of the data. At the bottom of fig. 22, the data are plotted versus a combined parameter, $S = (N_{dir}(75)\text{-}2) \cdot L_{dir}(25)/20$. In this parameter, the data exhibit a nearly exponential decrease. Assuming the decrease of the background dominated events to continue at higher S values, one can calculate the probability that the separated events are fake events. The probability to observe one event at $S \geq 70$ is 15%, the probability to observe 3 events is only $6 \cdot 10^{-4}$.

Fig. 23 shows the distribution when $|\vec{v}|$ and $L_{dir}(25)$ are relaxed. The 3 events are marked by arrows. There is one additional event at high $L_{dir}(25)$, which, however, has a somewhat too small $|\vec{v}|$. The 3 events fall into the region populated by MC generated atmospheric neutrino events passing the same cuts (bottom of fig. 23). We attribute the lack of experimental events between $L_{dir}(25) \sim$ 150–200 to statistical fluctuations.

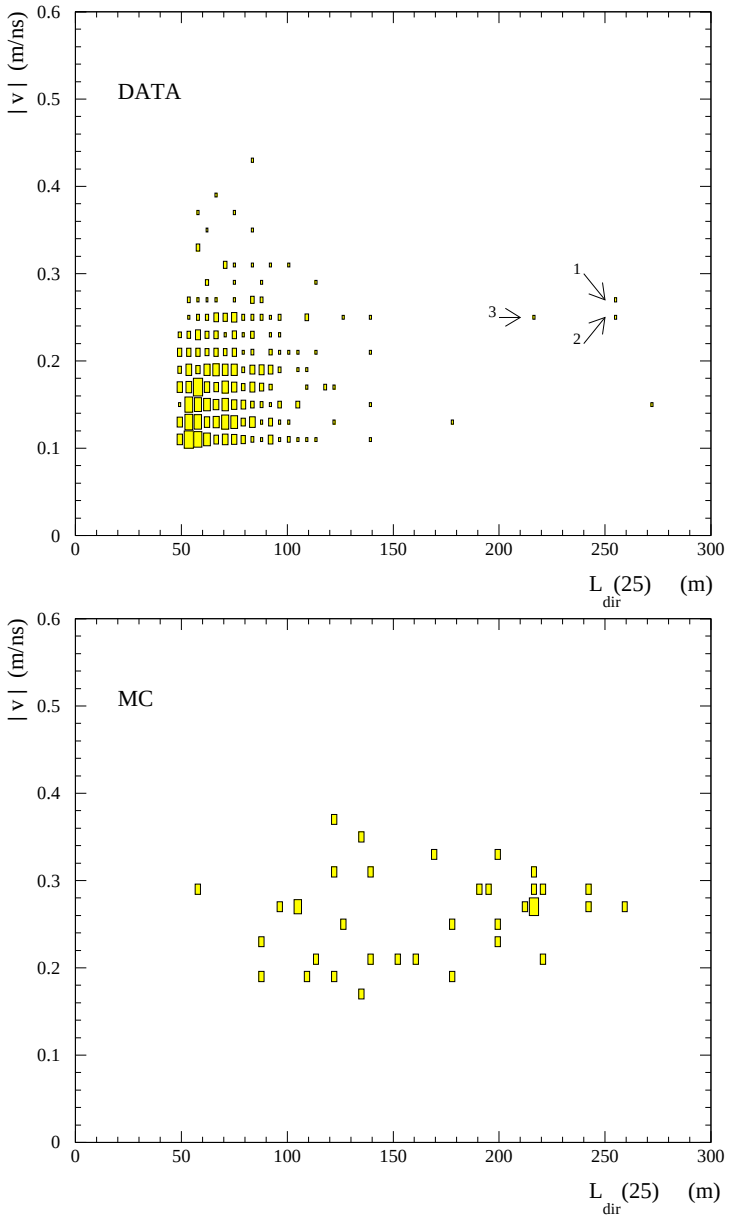

Figure 23: Distribution in parameters $|\vec{v}|$ vs. $L_{dir}(25)$, after application of all cuts with the exception of cuts 2 and 7, which have been relaxed. *top:* experimental data, *bottom:* signal Monte Carlo sample

Due to CPU limitation we could not check the agreement between experimental data and atmospheric muon MC down to a $8.9 \cdot 10^{-9}$ reduction. However, down to a reduction of 10^{-5}, the disagreement does not exceed a factor of 3. A less conservative estimate of the accuracy of the

signal prediction can be obtained by replacing all dedicated cuts for $\theta > 90^o$ by the complementary cuts for $\theta < 90^o$. We observed a better-than-10% agreement between experimental data and MC after all cuts. In conclusion we estimate the uncertainty in the prediction of upward muon neutrinos to be about a factor 2.

Table #1 summarizes the characteristics of the neutrino candidates identified in the two analyses.

Table 1: Characteristics of the events reconstructed as up-going muons

event ID →	147 742	4 706 879	2 324 428	8 427 905
N_{OM}	13	14	15	8
N_{string}	3	4	3	2
$\log(\mathrm{L}/(N_{hit}-5))$	-8.3	-8.5	-8.0	-11.2
θ_{rec}, degrees	168.7	165.9	166.7	175.4
ϕ_{rec}, degrees	45.8	274.2	194.1	–

We conclude that tracks reconstructed as up-going are found at a rate consistent with that expected for atmospheric neutrinos. The three events found in the second analysis are well separated from background proving that, even with a detector as small as AMANDA-B4, neutrino candidates can be separated within a limited zenith angle interval. Meanwhile, a few tens of clear neutrino events have been identified with the more powerful AMANDA-B10 telescope. They will be the subject of a forthcoming paper.

10 Conclusions

We have described the design, operation, calibration and selected results of the prototype neutrino telescope AMANDA-B4 at the South Pole.

The main results can be summarized as follows:

- AMANDA-B4 consisting of 80 optical modules (+ 6 OMs for technology tests) on 4 strings has been deployed at depths between 1.5 and 2.0 km in 1996. Seven of the OMs failed during refreezing. We have developed reliable drilling and instrumentation procedures allowing deployment of a 2 km deep string in less than a week. In the mean time the detector has been upgraded to 302 (AMANDA-B4, 1997) and 424 (1998) optical modules.
- The ice properties between 1.5 and 2.0 km are superior to those at shallow depths. The absorption length is about 95 m and the effective scattering length about 24 m.
- The original calibration accuracy reached for geometry and timing of AMANDA-B4 was about 2 m and 7 nsec, respectively. With the upgrade to 10 strings, these values have been improved to 0.5 - 1.0 m and 5 nsec.
- We have developed proper methods for track reconstruction in a medium with non-negligible scattering. With tailored quality cuts, the remaining badly reconstructed tracks

can be removed. The quality of the reconstruction and the efficiency of the cuts improve considerably with increasing size of the array.

- Geometry and tracking accuracy of AMANDA can be calibrated with surface air shower detectors. The mismatch between showers detected in the SPASE air shower array and muons detected with AMANDA is about 4 degrees, in agreement with Monte Carlo estimates of the angular accuracy.

- The measured angular spectrum of the intensity of atmospheric muons is in good agreement with other experiments and with model calculations.

- First neutrino candidates have been separated with AMANDA-B4. The identification of upward muon candidates with an array of only 73 operating 8-inch PMTs is a demonstration that deep antarctic ice is an adequate medium for doing neutrino astronomy.

Amanda-B4 is a first step towards a large neutrino telescope at the South Pole. A ten-string array, AMANDA-B10, has been taking data since 1997. Presently, B10 data are analyzed, and tens of clear neutrino candidates have been extracted, with a threshold of typically 50 GeV. The construction of AMANDA-II, a 30 000 m^2 array, is underway. The long-term goal of the collaboration is a cube kilometer detector, ICECUBE.

11 Acknowledgments

This research was supported by the U.S. National Science Foundation, Office of Polar Programs and Physics Division, the University of Wisconsin Alumni Research Foundation, the U.S. Department of Energy, the U.S. National Energy Research Scientific Computing Center, the Swedish Natural Science Research Council, the Swedish Polar Research Secretariat, the Knut and Alice Wallenberg Foundation, Sweden, and the Federal Ministery for Education and Research, Germany. C.P.H. acknowledges the support of the European Commission through TMR contract No. ERBFMBICT91551.

We thank the Polar Ice Coring Office, PICO, for bore hole drilling, and the Antarctic Support Associates, ASA, as well as the staff of the Amundsen Scott station for support and assistance. We gratefully acknowledge help from the SPASE collaboration, Leeds University, and the U.K. Particle Physics and Astrophysics Research Council.

References

[1] T.Gaisser, F.Halzen, T.Stanev, Physics Report **258** (1995) 174.

[2] See e.g. A.Bottino et al., Astropart.Phys. **2** (1994) 77, and
L.Bergström and J.Edsjö, astro-ph/9607237.

[3] F.Halzen, J.Jacobsen, E.Zas, Phys.Rev. **D49**, (1994) 1758.

[4] J.L.Thorn et al., Phys.Rev. **D46** 4846, and
Z.Djilkibaev, Proc. Int. Workshop on Simulation and Analysis Methods for Large Neutrino Telescopes, Zeuthen, Germany (1998).

[5] I.A.Belolaptikov et al., Astropart.Physics **7** (1997) 263.

[6] P.Askebjer et al., Science **267** (1995) 1147.

[7] AMANDA Collaboration, J.Glaciology **41** (1995) 445.

[8] Project Description Baikal 92-03 (DESY 1992), and V.Balkanov et al., astro-ph/9903342.

[9] DUMAND II Proposal HDC-2-88 (Hawaii, 1988).

[10] S.Matsuno et al., Nucl.Instr. and Methods **A276** (1989) 359.

[11] L.K.Resvanis et al., Proc. of High Energy Neutrino Astrophysics Workshop, Hawaii, X.Tata editors, World Scientific (1992), 325.

[12] ANTARES Proposal 1997: astro-ph/9707136.

[13] D.M.Lowder et al., Nature **353** (1991) 331.

[14] Yu.F.Barkov et al., Moscow Glaciological Research Publication (1984).

[15] R.Wischnewski et al., Proc. 24th Int. Cosmic Ray Conf., Rome, Italy, **1** (1995) 658.

[16] R.Porrata et al., Proc. 25th Int. Cosmic Ray Conf., Durban, South Africa, **7** (1997) 237.

[17] D.Lowder and K.Woschnagg, Proc. Int. Workshop on Simulation and Analysis Methods for Large Neutrino Telescopes, Zeuthen, Germany (1998).

[18] Y.He and B.Price, Geophys.Res.Lett. **25** (1998) 2845.

[19] S.N.Boziev et al., INR Preprint P-0630, Moscow, Russia (1989).

[20] E.Scapparone, Proc. Int. Workshop on Simulation and Analysis Methods for Large Neutrino Telescopes, Zeuthen, Germany (1998), and references therein.

[21] L.Volkova, Sov.J.Nucl.Phys **31** (1980) 784.

[22] W.Lohmann, R.Kopp, R.Voss, CERN 85-03 (1985).

[23] S.Hundertmark, Proc. Int. Workshop on Simulation and Analysis Methods for Large Neutrino Telescopes, Zeuthen, Germany (1998).

[24] V.J.Stenger, University of Hawaii, HDC-1-90. See also J.Jacobsen, PhD thesis, http://alizarin.physics.wisc.edu/jacobsen.

[25] A.Bouchta, PhD thesis, Stockholm 1998, USIP Report 98-07.

[26] C.Wiebusch, Proc. Int. Workshop on Simulation and Analysis Methods for Large Neutrino Telescopes, Zeuthen, Germany (1998).

[27] D.Pandel, Diploma thesis, Humboldt-University Berlin, 1996.

[28] C.Wiebusch et.al., Proc. 25th Int. Cosmic Ray Conf., Durban, South Africa, **7** (1997) 13.

[29] A.Biron et al., Upgrade of AMANDA-B towards AMANDA-II, DESY PRC 97/05, http://www.ifh.de/amanda/publications/proposal

[30] J.Dickinson et al., Proc. 25th Int. Cosmic Ray Conf., Durban, South Africa, **5** (1997) 233.

[31] J.Dickinson et al., Proc. 25th Int. Cosmic Ray Conf., Durban, South Africa, **5** (1997) 229.

[32] T.Miller et al. Proc. 25th Int. Cosmic Ray Conf., Durban, South Africa, **5** (1997) 237.

[33] J.Beaman et al., Phys. Rev. **D48** (1993) 4495.

[34] T.K.Gaisser et al., Proc. 24th Int. Cosmic Ray Conf., Rome, Italy, **1** (1995) 938.

[35] S.Hundertmark, PhD thesis, Zeuthen 1998.

[36] V.Blobel, Unfolding in High Energy Physics, DESY84-118, 1984, and Regularized Unfolding for High Energy Physics Experiments, Opal Note TN361, 1996.

[37] G.Zech, Comparing Statistical Date to Monte Carlo Simulation: Parameter Fitting and Unfolding, DESY-95-113, June 1995

[38] E.Bugaev et al., Phys.Rev. **D58** (1998).

[39] C.Allkover, Cosmic Rays on Earth, Karlsruhe 1984.

[40] W.Rhode, PhD thesis, Wuppertal 1993.

[41] M.Crouch et al., Phys.Rev. **D18** (1978) 2239.

[42] C.Berger et al., Phys.Rev. **D40** (1989) 2163.

[43] M.Ambrosio et al., Phys.Rev. **D52** (1995) 3793.

[44] P.Lipari, Astropart.Phys. **1** (1993) 1995.

[45] J.Babson et al., Phys.Rev. **D42** (1990) 41.

[46] T.Gaisser, Cosmic Rays and Particle Physics, Cambridge University Press, 1990.

[47] S.Ritz and D.Seckel, Nucl.Phys **B304** (1988) 877.

[48] E.Dahlberg, USIP Report 98-02, Stockholm 1997.